UNIVERSITY OF CALIFORNIA, MERCED

Synthesis of Iron Germanium Telluride and Ni Doped Iron Germanium Telluride through Chemical Vapor Deposition

A master's thesis submitted in partial satisfaction of the
requirements for the degree
Master of Science

in

Physics

by

Lutfun Nahar

Committee in charge:

Associate Professor Michael Scheibner, Chair
Professor Sayantani Ghosh
Assistant Professor Hui Cai

2023

The master's thesis of Lutfun Nahar is approved,
and
it is acceptable in quality and form for publication
on microfilm and electronically:

(Professor Sayantani Ghosh)

(Assistant Professor Hui Cai)

(Associate Professor Michael Scheibner, Chair)

University of California, Merced

2023

TABLE OF CONTENTS

LIST OF FIGURES

LIST OF TABLES

ACKNOWLEDGEMENTS

I would like to express my heartfelt gratitude to everyone who supported me throughout my master's thesis journey.

First and foremost, I am deeply indebted to my thesis advisor, Hui Cai, for his unwavering support and mentorship. His expertise and insightful feedback played a pivotal role in shaping the direction of this research. I am truly grateful for his guidance and the time spent discussing and refining this work.

I would like to extend my appreciation to the committee chair, Michael Scheibner for his feedback, suggestions, and commitment to the academic rigor of this thesis. I am also grateful to Prof Sayantani Ghosh for contributing her time and effort to this work. Their expertise and diverse perspectives greatly enriched the quality of this research.

My friends and colleagues, Bamidele Onipede and Matthew Metcalf deserve special mention for their patience and understanding during my intense periods of research and writing. Their support and camaraderie were a source of inspiration.

I am profoundly grateful to my parents, Sayeda Arifa and Md Amzad Hossain, for their unwavering love, support, and sacrifices throughout my academic journey. Your inspiration has been the driving force behind my academic pursuits. I should give special thanks to my husband, Sahadat for providing a caring and supportive environment during the accomplishment of the entire work. I am also grateful to my family members for their constant encouragement throughout this process. Their love and support were my pillars of strength during the challenging phases of this journey.

Lastly, I extend my appreciation to the faculty, staff, and resources at the University of California, Merced for providing an enriching environment for learning and research.

Thank you.

Lutfun Nahar

VITA

2011	B. S. in Physics, Jahangirnagar University, Dhaka, Bangladesh
2012	M. S. in Physics, Jahangirnagar University, Dhaka, Bangladesh
2013-2019	Lecturer in Physics, Institute of Natural Sciences, United International University, Dhaka, Bangladesh
2019-2023	Graduate Teaching Assistant, University of California, Merced
2022-2023	Basic Training on Atomic Force Microscope, Glove Box Training, Lab Safety Fundamentals, Hazmat Spill Response and DOT Awareness, Fire Safety Training, Laser Safety in the Lab, Compressed Gas Training, and Hazardous Waste Management
Summer 2022	Fabrication of Heterostructures at Transfer Station, Raman Mapping on the twisted bilayer of graphene covered by hexagonal boron nitride (hBN)
Fall 2022	Design of Experiments (DOEs) on the Chemical Vapor Deposition (CVD) Project of Iron Germanium Telluride (FGT)
Spring 2023	Synthesis of FGT at the CVD station, Raman Spectra Measurements at the Raman Spectrometer, XPS Depth Profiling of FGT at the X-ray Photoelectron Spectrometer
Summer 2023	Synthesis of Ni Doped FGT at the CVD station, XPS Depth Profiling of Ni Doped FGT at the X-ray Photoelectron Spectrometer
Fall 2023	XPS Data Analysis of XPS spectra of FGT and Ni Doped FGT using XPSPeakFit and Origin
2023	M. S. in Physics, University of California, Merced

PUBLICATIONS

Lutfun Nahar, "Ion-acoustic K-dV and mK-dV solitons in a degenerate electron-ion dense plasma,", *Physics of Plasmas*, 20, 022304, 2013.

ABSTRACT OF THE DISSERTATION

Synthesis of Iron Germanium Telluride and Ni Doped Iron Germanium Telluride through Chemical Vapor Deposition

by

Lutfun Nahar
Master of Science in Physics

University of California Merced, 2023

Associate Professor Michael Scheibner, Chair

The purpose of this work is to use Chemical Vapor Deposition (CVD) to produce Iron Germanium Telluride (FGT) and Ni-doped Iron Germanium Telluride. Due to its high Curie temperature, this layered van der Waals material has attracted a lot of attention and is an excellent choice for devices in spintronics and other domains. To create novel materials with a variety of physical characteristics, researchers are currently learning how to create homogeneous, atomically thin layers and govern them. Reducing a system's dimensions results in less phase space and screening, which enhances quantum effects and increases correlations. This explains why low-dimensional systems often exhibit special optical, magnetic, and electrical characteristics. These days, doping with transition metal chalcogenides, such as nickel (Ni) and cobalt (Co), is frequently observed among researchers. It has been discovered that doping Ni into Iron Germanium Telluride can dramatically alter the material's magnetic characteristics, including conductivity, magnetic permeability, and Curie Temperature (T_C), and others. Therefore, it is imperative to investigate the properties of magnetic materials such as FGT in the presence of dopants, defects, and other external control parameters at different layers, since this could lead to novel directions for future discoveries in science.

In this work, the successful synthesis of Iron Germanium Telluride (Fe_5GeTe_2) has been done from a 2 : 1 : 0.1 molar ratio of $FeCl_2$, Ge, and KI salt using a

cascaded space CVD method. CVD synthesis of Fe_5GeTe_2 is new where researchers found a Curie temperature of up to 280 K and the highest conductivity of $5.445 \times 10^5 \Omega^{-1}m^{-1}$ $(0.8THz)$ and $5.778 \times 10^5 \Omega^{-1}m^{-1}$ $(1.7THz)$ with THz spectroscopy experiments. The chemical species and quantification of elements have been done by X-ray photoelectron spectroscopy (XPS). The XPS depth profiling reveals that the percentage concentration can vary from the surface ($Fe_{2.15}GeTe_{0.37}$) to the higher etching level ($Fe_{4.73}GeTe_{2.13}$) with changes of the area of the elemental peaks. The iron ($Fe2p_{1/2}$ and $Fe2p_{3/2}$) and Tellurium (Te) show spin-orbit splitting, where no spin-orbit splitting was identified in Germanium (Ge). Besides, there is a mixed-valence oxidation state in iron (Fe^{2+} and Fe^{3+}). The percentage concentration of Germanium decreases with an increase in the concentration of tellurium (Te) revealing a possibility of Te-terminated atomic structure of FGT.

To produce the Ni-doped Iron Germanium Telluride, a small percentage of Ni powder was added to the mixture of $FeCl_2$, Ge, and KI powder to prepare a $2:1:0.2:0.1$ ($FeCl_2 : Ge : Ni : KI$) molar ratio and then selected for XPS depth profiling. A significant decrease in the $\frac{Fe^{2+}}{Fe^{3+}}$ value before etching indicates Ni is substituting to the Fe^{2+} atom. The Ni spectra ($Ni2p_{1/2}$ and $Ni2p_{3/2}$) are similar to the NiTe with some changes in their peak positions. All component elements show spin-orbit splitting. The percentage concentration indicates a strong Ge on the surface ($Fe_{5.55}Ni_{1.3}TeGe_{5.64}$) which decreases to the higher etching level ($Fe_{3.6}Ni_{0.47}TeGe_{1.95}$). Following this, the atomic structure and properties of the material could be changed. The Te spectra are almost the same as Fe_5GeTe_2 except a Te suboxide peak at etch 7.

In future, the thickness of both undoped and doped films should be measured by Atomic Force Microscope. Magnetic force Microscope measurements could reveal new magnetic domains in the sample. The crystal structure and properties of the material should be studied by structural, electronic, and magnetic characterization. Overall, the synthesis of FGT and Ni doped FGT could reveal new significant properties of the materials which could be used for spintronic applications.

Chapter 1

Introduction

1.1 Two Dimensional Magnets

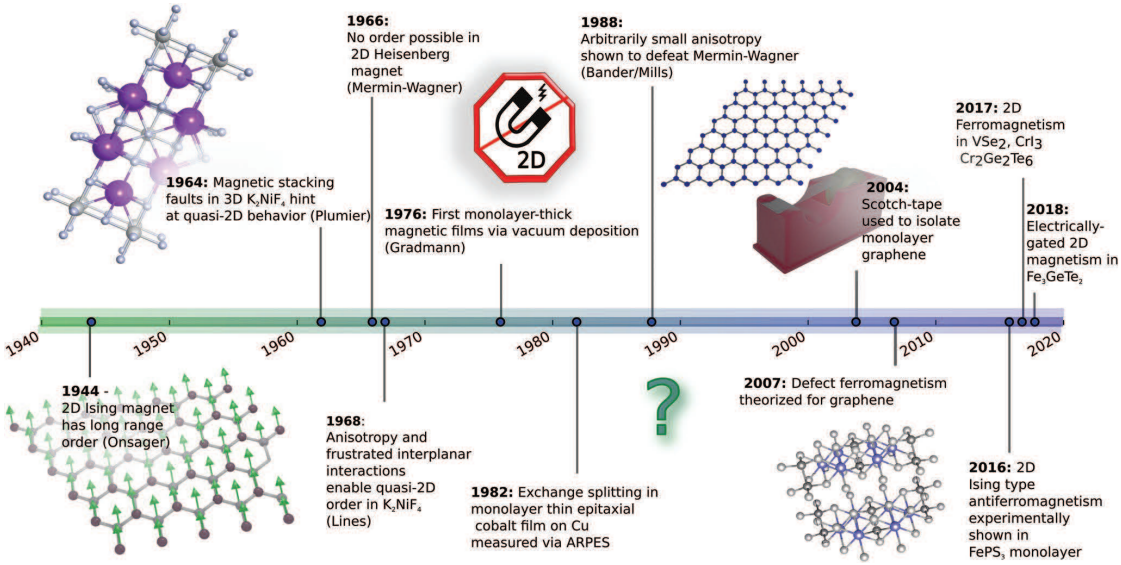

Figure 1.1: Timeline of some important theoretical and experimental results on 2D magnetism starting from Onsager's solution (1994) to the discovery of intrinsic 2D vdW materials (2016) [1].

Since the discovery of magnetism in ancient times, two-dimensional magnets have received enormous study attention due to their widespread applications in next-generation information technology. Magnetic recording and storage devices for computers and audio and video systems are some of the most esoteric uses of

magnetism. GMR devices became prevalent in computer hard disk drives about ten years after discovering interlayer exchange coupling and the associated giant magnetoresistance (GMR) effect in magnetic multilayers. They are also essential for spintronics, where information is carried by electron spin rather than charge to accelerate data processing [2]. The discovery was made in 2017 when 2D magnetism was confirmed in thin films of CrI_3 and $CrGeTe_3$. Following this discovery, ferromagnetism in 2D Fe_3GeTe_2 (FGT) was immediately reported in 2018. These 2D magnets have revealed intriguing behaviors, such as layer-dependent magnetism in CrI_3 and room-temperature ferromagnetism in FGT with ionic gating as shown in 1.1, but most of them are unstable and made by mechanical exfoliation, which is time-consuming and lose control over sample size and thickness, preventing further investigations and application. Recent developments in the controlled chemical vapor deposition (CVD) of TMCs have drawn enormous research attention to the research of CVD-grown magnetic transition metal chalcogenides (TMCs). The advantages of CVD over other synthesis methods, together with its large scale, good quality, and high tunability, have proven it the method of choice for producing a variety of 2D materials [3].

1.2 Historical Models and Exchange Interaction of Interacting Magnetic Moments

The interaction between the nearby spins is what creates the ordered organization of magnetic moments over macroscopic length scales and a spontaneous violation of time-reversal symmetry. The conditions that favor particular relative orientations between them can be created via this process, often referred to as exchange coupling. When the temperature is zero (T), the local order can span macroscopic length scales. Long-range order is lost above the critical temperature (T_c) due to the tendency of thermal fluctuations to cause magnetic moments in nearby regions to be out of alignment. Indeed, the efficiency of thermal fluctuations, which is controlled by a few general parameters, determines whether a system experiences a phase transition at a finite T_c. Dimensionality is one of

the parameters which plays an essential role in determining the impact of thermal fluctuations on the critical behaviour of many-body systems [4, 1].

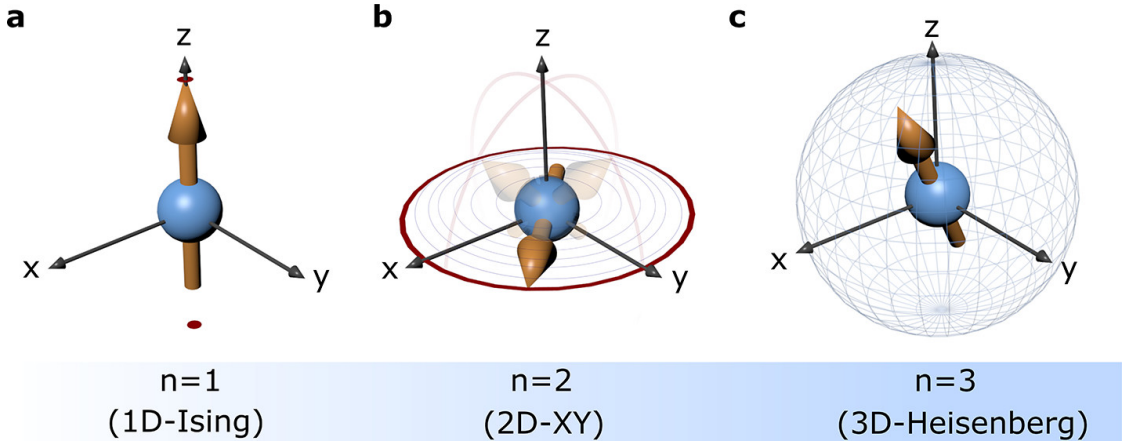

Figure 1.2: Ising, XY, and Heisenberg model.

In a three-dimensional (3D) system, the magnetic phase transition can always happen at a finite temperature, whereas in a one-dimensional (1D) system, long-range order is only conceivable at T = 0. A two-dimensional (2D) system presents a more complicated issue. The existence of long-range magnetic order in a 2D system at any finite temperature largely depends on the quantity n of pertinent spin components, also known as spin dimensionality, which is defined by the system's physical properties, such as the degree of magnetic anisotropy. The Mermin-Wagner theorem argues that thermal fluctuations, which occur in 2D systems at a finite temperature when the spin dimensionality is 3, or the isotropic Heisenberg model, destroy long-range magnetic order. This theorem concentrates for definiteness on finite-range exchange interactions. This is because the continuous symmetry of the isotropic model causes zerogap long-wavelength excitations (spin waves), which have detrimental impacts on magnetic order and have a finite density of states in 2D. On the contrary, the exact solution by Onsager of the 2D Ising model shows that a phase transition to a magnetically ordered phase occurs at $Tc > 0$ when n = 1 where the anisotropy of the system, favoring a specific spin component, opens a gap in the spin-wave spectrum, therefore suppressing the thermal fluctuations effect. For planar 2D XY model having dimensionality

(n = 2), there is no transition to long-range order, although the susceptibility diverges below a finite temperature [1, 4]. A simple and yet successful strategy that allows interpolation between the above scenarios and a description of more realistic situations relies on the use of a generalized Heisenberg spin Hamiltonian:

$$H = -\frac{1}{2}\sum_{i,j}(J_{i,j}\boldsymbol{S_i}.\boldsymbol{S_j} + \Lambda S_i^z S_j^z) - \sum_i A(S_i^z)^2 \tag{1.1}$$

Here, J stands for the exchange coupling between spins S_i and S_j on adjacent sites, favoring either the ferromagnetic order ($J > 0$) or the antiferromagnetic order ($J > 0$), while A and Λ stand for the respective "on-site" and "intersite" magnetic anisotropies. This model recovers, within certain bounds, the idealized theoretical scenarios while capturing the key characteristics of the majority of experimental systems. In instance, the Ising ($n = 1$) or XY ($n = 2$) models can be recovered in the case of substantial easy-axis or easy-plane anisotropy, but the isotropic Heisenberg model ($n = 3$) corresponds to the absence of magnetic anisotropy ($A \approx 0$ and $\Lambda \approx 0$). In the case of dipole-dipole interactions, which may be partially explained in terms of a renormalization of the onsite anisotropy, this model can effectively account for some subtle effects. Depending on the values of J, and A as well as the presence of additional magnetic interactions, a wide variety of physical events are anticipated [1, 4]. With the recent advancements in the manufacture of monolayers by exfoliation, chemical vapor deposition (CVD), and other methods, the knowledge gathered in the 1990s on magnetic layered compounds with vdW bonding is now opening up new possibilities.

1.2.1 Iron Germanium Telluride: A Two-Dimensional Van der Waals Ferromagnet

Iron Germanium Telluride (Fe_3GeTe_2) is a van der Waals ferromagnet with a Curie temperature (T_C) of about 220-230 K [5]. It is an itinerant ferromagnet with strong electron correlation effects and Kondo lattice physics [6]. The material has a reasonably high perpendicular magnetic anisotropy and is known to exhibit 2D itinerant magnetism [5]. Recent studies have shown that monolayer Fe_3GeTe_2 is a

robust 2D itinerant ferromagnet with strong out-of-plane anisotropy [5, 6, 7]. The thickness-dependent studies reveal a crossover from 3D to 2D Ising ferromagnetism for thicknesses less than 4 nm (five layers), accompanied by a fast drop of the Curie temperature from 207 K down to 130 K in monolayer [5].

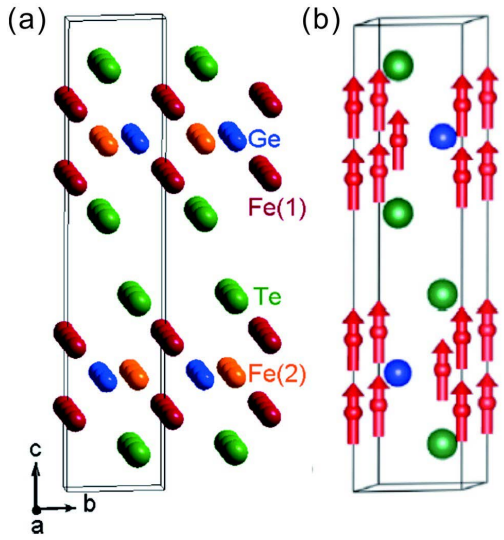

Figure 1.3: Intrinsic structural and magnetic properties of Fe_3GeTe_2 compounds grown by different methods [7].

Fe_3GeTe_2 also features a layered hexagonal crystal structure (space group P_{63}/mmc), where the Fe_3Ge slabs are sandwiched between Te layers. The vdW gap separates the two adjacent Te layers, as shown in Figure 1.3 [7]. Fe atoms occupy two different sites in the crystal lattice, indicated as Fe(1) and Fe(2). The Fe(1) site is fully occupied, whereas a deficiency of Fe on the Fe(2) site easily forms during sample growth. Different forms of Fe_3GeTe_2 have been grown, such as polycrystal, single crystal [7], and thin films by molecular beam epitaxy, mechanical exfoliation and chemical vapor deposition where the lattice parameters and magnetic properties strongly depend on the Fe concentration and the growth conditions.

Magnetic studies suggest that Fe_3GeTe_2 is a strongly correlated itinerant ferromagnet with highly anisotropic magnetic behavior. Transport measurements suggest the metallic behavior of the compound.

Additional nominal Fe doping decreases the lattice constant c while increasing

the constant a. With increasing Fe composition, the T_C dramatically increases e.g. Fe_5GeTe_2. However, the Fe(2) vacancy cannot be completely avoided even in the optimized conditions, and the highest T_C value of Fe_3GeTe_2 of a single crystal reported in the literature is $\approx 230K$ [7]. The Fe_3GeTe_2 single crystal exhibits strong out-of-plane easy magnetization anisotropy with a T_C of $\approx 230K$. Recently, it was possible to modulate the Curie temperature (T_c) of Fe_xGeTe_2 (FGT) from 230 K (Fe_3GeTe_2) to 280 K (Fe_5GeTe_2), close to the ambient temperature [5]. The highest conductivity of $5.445 \times 10^5 \Omega^{-1}m^{-1}$ ($0.8THz$) and $5.778 \times 10^5 \Omega^{-1}m^{-1}$ ($1.7THz$) was measured with THz spectroscopy experiments [5].

Compared with other 2D vdW magnets mentioned earlier, Fe_xGeTe_2 is a a promising candidate for future spintronic applications benefiting from its superior stability, relatively high Curie temperature, and very strong perpendicular anisotropy, which are very critical for spin-based technology [7]. Doping in Iron Germanium Telluride (FGT) can change its magnetic properties like magnetic permeability and T_c which has been discussed in detail in chapter 4.

1.2.2 Applications

Iron Germanium Telluride has potential applications in spintronics, magnetic storage, and other electronic devices [2]. However, more research is needed to fully understand its properties and potential applications. Based on the information available, the applications of Iron Germanium Telluride can be categorized as follows:

Spintronics: Iron Germanium Telluride has potential applications in spintronics due to its strong electron correlation effects and Kondo lattice physics [2].

Magnetic storage: Iron Germanium Telluride has potential applications in magnetic storage due to its van der Waals ferromagnetism and reasonably high perpendicular magnetic anisotropy [2].

Electronic devices: Iron Germanium Telluride has potential applications in other electronic devices due to its 2D itinerant magnetism and strong out-of-plane anisotropy [2].

However, more research is needed to fully understand the properties of Iron

Germanium Telluride and its potential applications in these fields.

Rajendran et al demonstrated a cascaded space confined chemical vapor deposition (CS-CVD) technique to synthesize 2D Fe_xGeTe_2 ferromagnets [5]. In this work, the weight fraction of iron (Fe) in the precursor controls the phase purity of the as-grown Fe_xGeTe_2. As a result, high-quality Fe_3GeTe_2 and Fe_5GeTe_2 flakes have been grown selectively using the CS-CVD technique. Curie temperature (T_C) of the as-grown Fe_xGeTe_2 can be up to $\approx$ 280 K, nearly room temperature. The thickness and temperature-dependent magnetic studies on the Fe_5GeTe_2 reveal a 2D Ising to 3D XY behavior. The results of this work indicate a scalable pathway for the direct growth and integration of 2D ternary magnets on CMOS-based substrates to develop spintronic memory devices.

Since a spintronic-based device favors Out of Plane (OOP) anisotropy over in-plane anisotropy because of factors like low spin switching current, thermal stability factor, etc., the 2D magnets with ultrathin thickness and OOP anisotropy are highly required. So far, the researchers have relied mainly on the chemical vapor transport (CVT) method to produce 2D magnet bulk single crystal and exfoliate it into atom-thin layers for device fabrications. However, the CVT method limits the application of 2D magnets due to layer control and scale-up production. Therefore, it is highly desirable to synthesize 2D magnets via scalable methods such as CVD onto complementary metal oxide-semiconductor (CMOS) compatible substrates like SiO_2/Si [5].

1.3 Synthesis Techniques

FGT can be produced following different synthesis techniques like sputtering, Liquid phase exfoliation, Chemical Vapor Transport, Chemical Vapor Deposition, and others [5, 8, 9, 10, 11, 12, 13, 14]. Although mechanical exfoliation can be used to prepare high-quality 2D materials, it cannot be used to fabricate large-area 2D materials with high yield and reproducibility. Therefore, an alternative fabrication method must be developed to synthesize 2D materials for practical applications in future electronics and optoelectronics. Chemical vapor deposition (CVD) has been

widely used to fabricate one-dimensional (1D) nanowires and nanotubes since the 1990s, as it offers good controllability, high yield at low cost. Therefore, it could provide a practical solution to fabricate large-area, uniform, and high-quality 2D materials for future applications. There are some advantages of CVD which is discussed below.

1.3.1 Chemical Vapor Deposition: A special synthesis method to produce Two Dimensional Nanomaterials

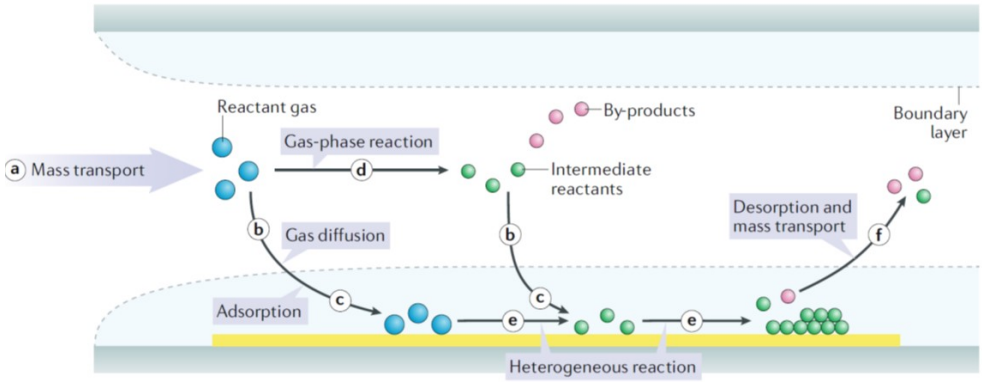

Figure 1.4: Schematic of general elementary steps of a typical CVD process. First, reactant gases (blue circles) are transported into the reactor (step a). Then, there are two possible routes for the reactant gases: directly diffusing through the boundary layer (step b) and adsorbing onto the substrate (step c); or forming intermediate reactants (green circles) and by-products (red circles) via the gas-phase reaction (step d) and being deposited onto the substrate by diffusion (step b) and adsorption (step c). Surface diffusion and heterogeneous reactions (step e) take place on the surface of the substrate before the formation of thin films or coatings. Finally, by-products and unreacted species are desorbed from the surface and forced out of the reactor as exhausts (step f) [15].

Chemical vapor deposition (CVD) is a process whereby a solid material is deposited onto a substrate through the chemical reactions of the gaseous species. It is an additive manufacturing technique. It is distinguished from the physical vapor deposition (PVD) processes, such as pulsed laser deposition, sputtering, and e-beam evaporation. Although CVD has some limitations such as the complexity of the chemical reaction and difficulty in determining the best parameters, it is popular for its many advantages in the synthesis of nanomaterials.

Advantages of CVD:

- good conformality in terms of uniform thickness of the coating
- a greater flexibility of using a wide range of chemical precursors, unlike PVD, which usually requires a large solid target
- relatively low deposition temperatures SiC (sublimate near $2700°C$) can be deposited at $1000°C$

$$CH_3SiCl_3 + (excessive)H_2 = SiC + 3HCl + (excessive)H_2 \tag{1.2}$$

- can control the crystal structure, stoichiometry, surface morphology and orientation of the CVD manufactured products
- deposition rate can be adjusted through reaction kinetics
- low-cost, does not normally require ultra-high vacuum

It is clear that in contrast to physical vapor deposition methods, such as evaporation and sputtering, CVD offers a clear advantage by relying on chemical reactions that enable tunable deposition rates as well as high-quality products. Recently, low-dimensional materials such as carbon nanotubes, graphene and 2D transition metal dichalcogenides (TMDs) have injected new vitality into the electronics industry and introduced more stringent requirements for successful CVD of these materials with high purity and fine structure. CVD allows the tuning of the structures and properties of the resulting products making it a popular technology for electronics, optoelectronics, surface modification and biomedical applications. A CVD system must have some basic requirements described by Sun et al [15] and sketched in figure 2.1.

1.3.2 Physical Fundamentals and Basic Requirements of a CVD System

Chemical Vapor Deposition (CVD) equipment is used to deposit thin films of materials on a substrate. The equipment consists of several parts, including:

Reaction chamber: This is the main part of the CVD equipment where the deposition process takes place. It is typically made of quartz or stainless steel and is designed to withstand high temperatures and corrosive gases.

Gas delivery system: This system delivers the precursor gases into the reaction chamber. It consists of several parts, including gas cylinders, mass flow controllers, and valves.

Vacuum system: This system is used to create a vacuum inside the reaction chamber before the deposition process begins. It consists of a vacuum pump and a pressure gauge.

Heating system: This system is used to heat the substrate and the precursor gases to the required temperature for the deposition process. It typically consists of a resistive heater or a radio-frequency (RF) coil.

Substrate holder: This is the part of the CVD equipment that holds the substrate in place during the deposition process. It is typically made of quartz or graphite and is designed to withstand high temperatures.

Quartzware: This includes all the quartz components of the CVD equipment, such as the reaction chamber, gas delivery system, and substrate holder. Quartz is used because it is transparent to the wavelengths of light used to monitor the deposition process.

Exhaust system: This system is used to remove the byproducts of the deposition process from the reaction chamber. It consists of a vacuum pump and a pressure gauge.

1.3.3 Tunability of Magnetic Properties of 2D magnets

Bulk chromium and iron-based chalcogenide crystals have attracted extensive research interest due to their robust magnetic ordering. It is important to note that Cr and Fe are frequently used due to their partially filled 3d orbitals, which are prone to exhibiting magnetic behaviors. A variety of magnetic behaviors, such as ferrimagnetism, ferromagnetism, and antiferromagnetism were proven to be present in Cr and Fe compounds by varying the composition of elements. The magnetic properties could also be different with the reduction of dimensionality.

It is also important to enhance the critical temperature in two dimensions for a variety of applications of 2D magnets. In some of the ultrathin layered magnets, efforts are currently being made to achieve room-temperature ferromagnetism. By electrostatically doping CrI_3-graphene vertical heterostructures, Shengwei et al.. showed that it is possible to regulate the magnetic characteristics of both monolayer and bilayer CrI_3. Doping in monolayer CrI_3 dramatically alters the saturation magnetization, coercive force, and Curie temperature, exhibiting stronger or weakened magnetic order with hole/electron doping. Surprisingly, in the absence of a magnetic field, electron doping in bilayer CrI_3 over triggers a transition from an antiferromagnetic to a ferromagnetic ground state. The outcome demonstrates a significantly doping-dependent interlayer exchange coupling, which permits reliable switching of magnetization in bilayer CrI_3 by low gate voltages. Strong charge doping has been shown to significantly raise the T_c of Cr_2GeTe_6 in semiconducting magnets from 60 K to around 200 K using ionic liquid gating [1, 4, 16].

It was shown in a different study that Cr_2Te_3 flakes behave differently from nearly every other 2D magnet that has been described so far, showing an anomalous increase in T_c as the flake thickness is decreased from 10 to 5.5 nm. The reason for this was doping and reconstruction of the Cr_2Te_3 surface, which led to a slightly changed stoichiometry and interlayer distance [1, 4, 16]. Iron Germanium Telluride (Fe_3GeTe_2) is a two-dimensional (2D) ferromagnetic metal that belongs to the family of 2D magnets. It is a van der Waals (vdW) ferromagnet with a reasonably T_C of about 220-230 K [17, 6]. In addition to a large out-of-plane anisotropy, evidence for strong electron correlation effects and Kondo lattice physics has been seen recently [17]. The material is a promising candidate for spintronic vdW heterostructures and for the study of controllable 2D itinerant Ising ferromagnetism [17].

1.4 Studies of FGT with Dopants in the Literature

Recently, Deng et al. reported the gate tunability of ferromagnetism in ultra-thin FGT [18]. Following the experiments of Deng et al.., Seung et al.. also demonstrated that the magnetic properties including T_c can be enhanced and manipulated by ionic gating. In order to understand the experiment, they investigated the effect of electron doping on the magnetic order. To simulate the experimental conditions, a Li atom is placed in the vicinity of the top surface of the FGT bi-layer. Note that the AFM to FM transition is induced by electron doping: in the high doping regime ($0.5 \leq 1/z_{Li} \leq 1$), the calculated E is positive [18]. Due to the high electropositivity of Li, electrons are transferred and doped onto FGT. According to Deng et al.. [18], the doping sites, lattice parameters (L_a), average magnetic moments of Fe^I and Fe^{II} atoms, magnetic moments of doped atoms ($M - M^{'}$), and the nearest-neighbor magnetic-coupling constants (J_0) between doped atoms and Fe atoms are listed in the table 1.1 below.

	Doping-SIte	L_a	$M - Fe^I$ (μ_B)	$M - Fe^{II}$ (μ_B)	$M - M^{'}$ (μ_B)	J_0 (meV)
V	Site-I	4.014	2.31	1.27	-0.27	-0.61
Cr	Site-I	4.004	2.31	1.25	2.52	11.72
Mn	Site-I	4.010	2.23	1.28	2.99	14.94
Pure	-	4.009	2.42	1.43	-	-
Co	Site-II	4.006	2.43	1.60	0.72	0.29
Ni	Site-I	3.975	2.25	1.27	-0.07	-2.36
Cu	Site-I	3.991	2.77	1.29	0	-
Zn	Site-I	4.014	2.26	1.39	0	-

Table 1.1: Doping sites, lattice parameters (L_a), average magnetic moments of Fe^I and Fe^{II} atoms, magnetic moments of doped atoms ($M - M^{'}$), and the nearest-neighbor magnetic-coupling constants (J_0) between doped atoms and Fe atoms

Another work based on first principles calculation was done by Shoozheng et al.. to study the formation energies of doping FGT with 3d transition metals which was in good agreement with experiment [18]. The characteristic equation to identify the formation energy (E_{form}) was calculated based on the following formula:

$$E_{form} = E_{pristine} - \mu_{Fe} + \mu_{3d} - E_{doped} \tag{1.3}$$

Here, E_{doped} and $E_{pristine}$ are the total energies of Fe_3GeTe_2, with and without the 3d dopants, respectively. μ_{Fe} and μ_{3d} are the chemical potentials for Fe and alien 3d atoms respectively, which represent the energy per atom of bulk phase. A high E_{form} means a high possibility for doping 3d atoms into Fe_3GeTe_2. This indicates that site I is more energetically favorable than site II for all 3d atoms, except for Co. They also found out of the variation of the valence electrons of doped 3d atoms and the magnetic moment of Fe atoms in Fe_3GeTe_2 [18]. The parameters like lattice parameters, magnetic moments, and magnetic coupling constants are listed in table 1. These results provide valuable information for future experimental studies of Fe_3GeTe_2 for spin nano-devices.

Some experimental works have been done by decreasing and increasing the Fe ratio on Fe_xGeTe_2. Besides, some experimental works also have been done by adding Nickel and Cobalt, the two elements highlighted in table I [19, 20, 21, 22].

Chapter 2

Method of Synthesis and Characterization Techniques

2.1 Method of Synthesis

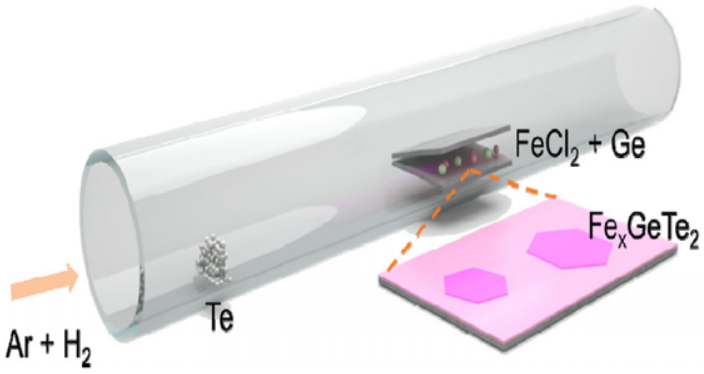

Figure 2.1: Schematic of the Confined Space Chemical Vapor Deposition (CSCVD) synthesis method to produce Iron Germanium Telluride (FGT) [5].

The solid precursors were powders of $FeCl_2$ (Sigma Aldrich), Ge (Sigma Aldrich), and Te (sigma Aldrich). Fe_xGeTe2 flakes were produced using a 1-inch quartz tube mounted with a Thermcraft single-zone CVD furnace. In order to speed up the formation of Fe_xGeTe_2 flakes, potassium iodide (KI) salt was utilized in combination with the precursors. In accordance with the studies by Rajendran et al.. [5], the Fe:Ge ratio was maintained at 1:1 and 2:1 to synthesize Fe_3GeTe_2

and Fe_5GeTe_2, respectively. The $FeCl_2$ (Sigma Aldrich), and Ge (Sigma Aldrich) precursors were mixed with the KI salt in an agate mortar. To Prepare a $2:1:0.1$ ($FeCl_2 : Ge : KI$) molar ratio 0.2535 gm $FeCl_2$ powder, 0.07263 gm Ge powder, and 0.0166 KI salt were mixed ($TotalMass = 0.3427gm$). For the Ni-doped sample, a new mixture of the same amount was prepared with an addition of 0.0138 gm Ni powder in the mixture to prepare a $2:1:0.2:0.1$ ($FeCl_2 : Ge : Ni : KI$) molar ratio. Only a small amount (e.g 1-2 drops if it was a liquid) is required to run one CVD reaction to produce the thin films. Samples from these two mixtures were selected for XPS and the results have been discussed later in chapters 3 and 4. The confined space was generated by some quartz beads and blocks of different heights like 1.5 mm, 2 mm, and 3 mm respectively. For this purpose, the quartz bead/block of desired height was placed between two SiO_2 substrates maintaining a good amount of gas flow in the system where the precursor mixture will be located. This confined space will be created on top of a quartz plate to put the precursors inside the center of the 1-inch quartz tube. The images of this experimental setup are shared in image 2.1. The cascaded substrate arrangement provided better space confinement and temperature control to obtain phase pure Fe_3GeTe2 and Fe_5GeTe2 [5]. The cascaded substrate arrangement inhibited the growth of unwanted binary phases of Fe, Ge, and Te. The vertical cascaded arrangement reduces the spatial zone of the reaction and ensures the proper mixing of all three elements (Fe, Ge, and Te). Avoiding the binary phase requires efficient space confinement, and the substrates' vertical cascaded arrangement serves this purpose. Moreover, the pure vapor phase of the precursors from the bottom stack of substrates will rise above the stacked substrates on top to provide better Fe_xGeTe_2 flakes by providing a plasma environment. Argon (Ar) gas was used to purge the furnace tube to limit the amount of oxygen in the quartz tube. CVD reaction was carried out in a temperature window of $550 - 600°C$. Hydrogen (H_2) gas (5 sccm) was coupled to aid the growth of FGT flakes. The ramping rate was kept at $50°C/min$, and the dwelling time was maintained at 1 minute.

2.2 Characterization Techniques

Using the CVD growth of graphene as an example, Sun et al.. described numerous characterization methods (listed in the table) to assess the macroscopic quality, atomic structure, electronic structure and purity of the resulting graphene. They followed a transfer process of the as-grown graphene from the metal catalytic substrate to a target substrate, which is necessary when assessing graphene quality because an appropriate substrate is important for some characterization techniques [15]. The description of some characterization techniques suitable for the samples deposited on a substrate by CVD are as follows.

2.2.1 Optical Microscopy

- Spatial Resolution: Micrometer or less.
- Property: Individual domain shapes, surface coverage, number of layers, grain boundaries, defects (wrinkles and folds) (wrinkles and folds).
- Advantages: Simple to operate, large-area characterization, non-destructive to the sample.
- Disadvantages: Low resolution; usually needs a suitable substrate.
- Background: Clearer images when choosing a suitable wavelength of light or adding an optical filter.

2.2.2 Raman Spectroscopy

- Spatial Resolution: Diffraction limit up to 100 nm.
- Property: Number of layers, defects, strain, doping.
- Advantages: Simple to operate, high sensitivity, spatially resolved distribution easily obtained by mapping the sample.
- Disadvantages: Qualitative only.

2.2.3 X-ray photoelectron spectroscopy

- Spatial Resolution: 100 micrometer.
- Property: Purity.
- Advantages: Surface-sensitive technique to analyze elemental composition and chemical state.
- Disadvantages: Low spatial resolution; no accurate quantification.
- Background: Detecting depth ranges from 1 to 10 nm, based on the photoelectric effect.

2.2.4 Atomic force microscopy

- Spatial Resolution: Nanometers or less.
- Property: Individual domain shapes, surface coverage, roughness, grain boundaries, number of layers.
- Advantages: High resolution, good environmental adaptability.
- Disadvantages: Scanned area is small, scanning speed is slow, unsuitable for samples with significant surface topography.
- Background: Sample surface must be clean, pollutants contaminate the tip and can result in virtual and/or false images.

Chapter 3

Synthesis of Iron Germanium Telluride

Two-dimensional (2D) ferromagnets with out-of-plane (OOP) magnetic anisotropy are potential candidates for realizing the next-generation memory devices with ultra-low power consumption and high storage density. However, a scalable approach to synthesize 2D magnets with OOP anisotropy directly on the complementary metal-oxide semiconductor (CMOS) compatible substrates has not yet been explored, which hinders the practical application of 2D magnets. With the thickness reduced to a single layer, Rajendran et al.. revealed how to directly synthesize two-dimensional (2D) ferromagnet Fe_xGeTe_2 magnets on a SiO_2 substrate using cascaded space chemical vapor deposition (CSCVD) [5].

3.1 Chemical Vapor Deposition of Iron Germanium Telluride

3.1.1 Method

I followed a slightly different procedure which I would like to mention as my second procedure to synthesize both Fe_3GeTe_2 and Fe_5GeTe_2 on the mica substrate. For this, I placed 8 mica substrates on top of the quartz plate where

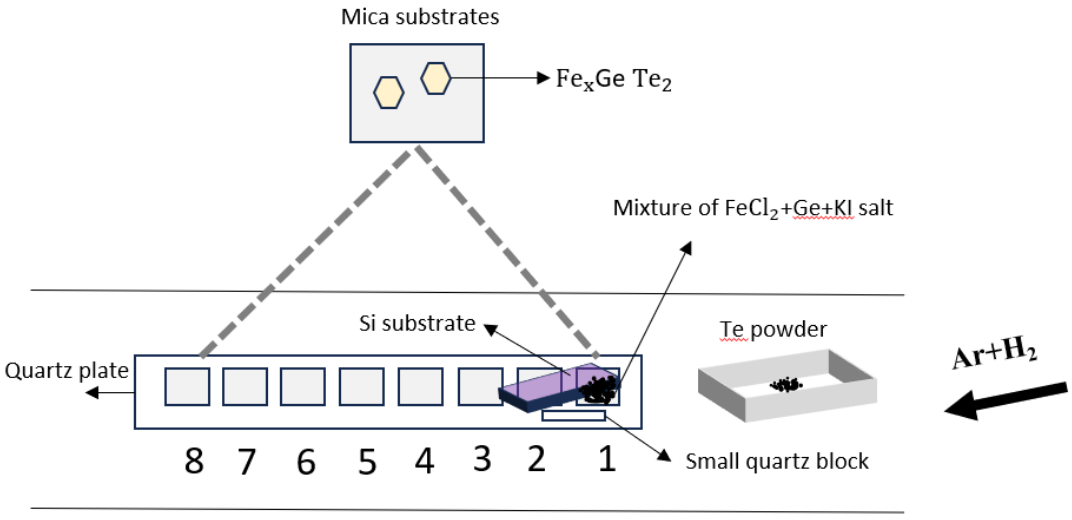

Figure 3.1: CVD Schematic F5GT

only the first substrate from the upstream side was loaded with the precursor mixture. The cascaded environment was maintained on top of the first two mica substrates using a 1.5 mm quartz block. To do this, I used a SiO_2 substrate as the ceiling but the growth happened at all the bottom mica substrates. To synthesize the doped samples, I added Ni powder (Sigma Aldrich) with a mixture of $FeCl_2$, Ge, and KI salt in a percentage of 5%, 10%, and 20% respectively. All doped samples were produced on mica substrates following the second procedure mentioned above, which is further discussed in chapter 4. All other parameters remained unchanged to grow both doped and undoped samples on mica substrate. A details description of optimizing the parameters is discussed in the next section.

3.2 Optimizing the Parameters

To reproduce the crystals of Fe_xGeTe_2 on a substrate via Chemical Vapor Deposition (CVD) we went through several challenges. Some of the parameters e.g. pressure, salt ratio were not revealed by Rajendran et al. In order to get rid of this problem and to optimize the parameters we had to run several CVD synthesis. The details of optimizing the parameters is shared in the next section. In this section, the results from different CVD runs have been discussed on the basis of the images and videos under the optical microscope. The parameters to control the CVD of FGT are as follows.

3.2.1 Temperature

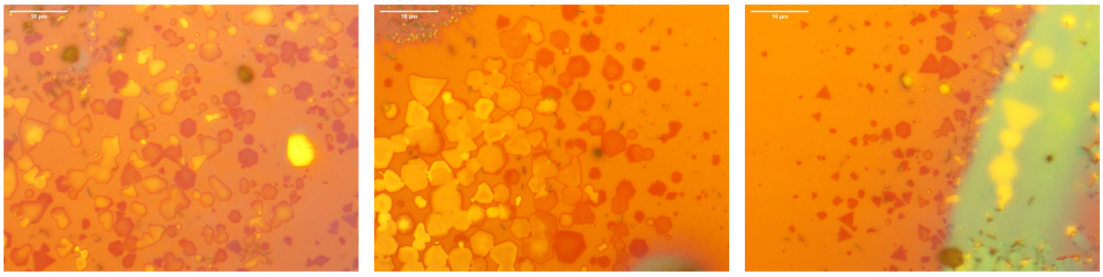

Figure 3.2: Thin films produced at 1.5 mm tilted confinement space on SiO_2 substrate. We are getting thinner crystals of multiple contrasts from 1.5 mm height (circular fashion). All images have a 10-micron scale bar.

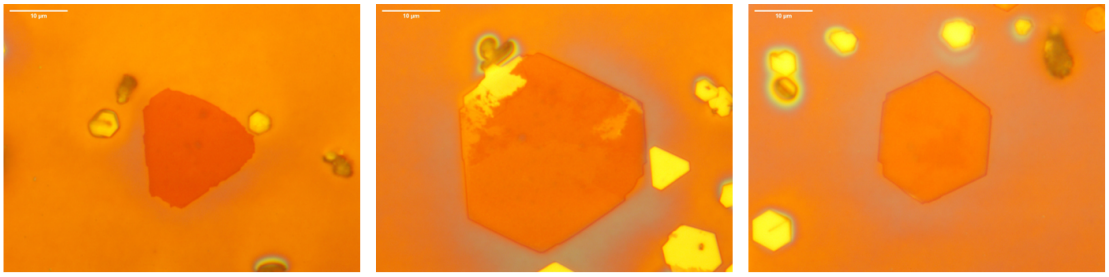

Figure 3.3: Thin films produced at 2mm tilted confinement space. Some thin crystals of large size are scattered throughout the entire substrate. All images have 10-micron scale bar.

Temperature plays an important role in the growth of crystals in a Chemical Vapor Deposition (CVD) process. Especially, it has significant impact in controlling the thickness of the two-dimensional materials. Besides, the lateral size of the crystal could also be affected by the crystal with the decrease in temperature of the Te precursor the lateral size of the films decrease on the mica substrates at the downstream side. For our CVD growth, the boundary condition for the formation of thin films is satisfied at $600°C$. However, more CVD productions are required to confirm this because CVD is a complex reaction, and other parameters could also be responsible for the crystal growth at different thicknesses. The other important parameters to control the thickness could be the height and orientation of the confinement. This is why, we should not change more than one parameter at a time to better identify the controlling parameter to make any changes in the CVD process. To observe the effect of temperature we ran 6 different CVDs in a temperature window of $550 - 610°C$ in a $10°C$ fashion with the ratio of $1 : 1 : 0.1$ $FeCl_2$, Ge, and KI salt respectively (used a quartz block of 1.5 mm). We observed an increase of the size of the crystals along with their edges with the increase of the crystals. Therefore, the appearance of the thinner flakes around the outer edges of the circular growth zones of the crystals is an effect of the increase of their size at $600°C$. The observance of smaller thin flakes became larger and prominent at $600°C$ and completely vanishes at $610°C$ on SiO_2 (Figure 3.1). Therefore, we select $600°C$ as the temperature to produce FGT at different layers with a 10 cm Te distance. Hexagonal shaped bulk crystals appeared at all temperatures on both SiO_2 and mica substrate.

3.2.2 Confinement Height and orientation

The growth of unwanted Fe, Ge, and Te binary phases was suppressed by a cascading substrate design. The vertical cascaded design confines the reaction's spatial zone. It ensures blending all three components (Fe, Ge, and Te) together. Efficient space confinement is essential to prevent the binary phases, which is enabled by the vertical cascaded arrangement of the substrates. The precursors' pure vapor phase from the substrates' bottom stack will ascend over the pile of

substrates on top and result in superior Fe_xGeTe_2 flakes by providing a plasma environment. To create the cascaded space in our growth we used beads of two different heights such as 2 mm and 3 mm at 600řC with a precursors' ratio of $1 : 1 : 0.1$ ($FeCl_2 : Ge : KI$). Bulk crystals of good shapes were observed with a small number of thin films at only 2 mm height. Although the setup of the vertical confined space between the two SiO_2 substrates with the beads was difficult and not worthy. However, this was much easier to create the vertical cascaded environment with the use of 1.5 mm quartz block ensuring the proper flow of Argon (Ar) and Hydrogen (H_2) into the system. In this way, we were able to get both bulk and thin films of Fe_3GeTe_2 as shown in figures 3.2 and 3.3.

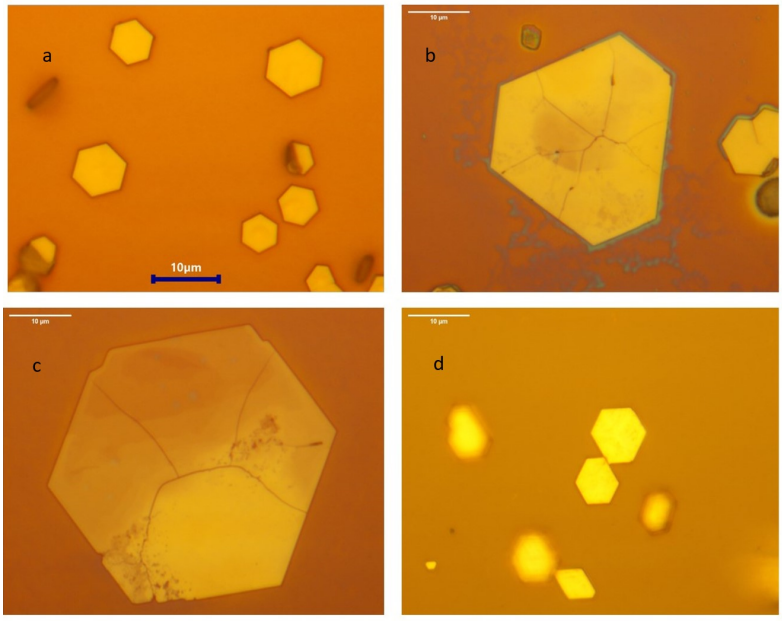

Figure 3.4: Bulk crystals appeared at $1 : 1 : 0.05$ salt ratio shown in figures b and c on SiO_2. Crystals in figure d are produced on top of mica substrate. All images have 10 micron scale bar.

3.2.3 Te distance

Another important parameter is the Te distance. We tried different Te distances at 5 cm, 10 cm, 11 cm, 12 cm, 13 cm, 14 cm, and 15 cm respectively from the zone center. The purpose of doing this is to select the best temperature for the Tellurium

precursor. Although bulk crystals were formed at all of the above mentioned Te distances, we observed the films at different layers from a 10 cm Te distance which is a good match from Rajendran et al.. [5].

3.2.4 Salt Ratios

After working with the temperature, the next parameter was the salt ratio. I tried six different salt ratios to grow FGT.

Table 3.1: Results from different salt ratios.

No	Molar Ratios ($FeCl_2 : Ge : KI$)	Results	Ratings
1	1 : 1 : 0	only a few crystals were observed around the entire substrate; others were residues	not good
2	1 : 1 : 0.01	good for large amounts of crystals; small crystals are found in the middle	good
3	1 : 1 : 0.05	good for big crystals; the biggest one was around $47 \cdot 5$ micrometer approximately (Figure 3.2(c))	good
4	1 : 1 : 0.1	good for large amounts of crystals, big crystals, both bulk and thin crystals	best
5	1 : 1 : 0.15	lumps increased, two growth zones	average
6	1 : 1 : 0.2	lumps increased, no single growth zone; only some scattered crystals	bad growth starts
7	1 : 1 : 0.5	all are lumps, bad crystals with some dots on top; But they are really big	bad

3.2.5 Summary

Table 3.2: Description of different parameters with results from CVD.

No	List of parameters	Description	Results
1	Temperature	$560-610^{\circ}C$ (in a $10^{\circ}C$ fashion), $650-850^{\circ}C$ (in a $50^{\circ}C$ fashion); [Dual time: 1 min; Height: 1.5 mm; Te distance: 10 cm; salt: 1 : 1 : 0.1 ($FeCl_2 : Ge : KI$)]	A combination of both bulk and thin films are found at $600^{\circ}C$ only; All others have bulk flakes; Bad growth started from $850^{\circ}C$ where bulk crystals are craked and some thin nanopartiicles appreared
2	Height of confinement	1.5 mm, 2 mm, 3.10 mm (using quartz beads), and unknown; [Dual time: 1 min; Te distance: 10 cm; Temp: $600^{\circ}C$; salt: 1 : 1 : 0.1 ($FeCl_2 : Ge : KI$)]	No thinner films at 3.10 mm height; the number of thin films are higher at 1.5 (figure 6a-c) mm height where 2 mm height (figure 6d-f) gives big thin films
3	Confinement Orientation	normal, tilted	Tilted is better for the formation of films at different layer
4	Salt Ratios	1 : 1 : 0 ($FeCl_2 : Ge : KI$), 1 : 1 : 0.01, 1 : 1 : 0.05, 1 : 1 : 0.1, 1 : 1 : 0.15, 1 : 1 : 0.2, and 1 : 1 : 0.5; [Dual time: 1 min; Te distance: 10 cm; Temp: $600^{\circ}C$; Height: 1.5 mm]	The results are in the salt chart
5	Te distance	5 cm, 10 cm, 15 cm; [Dual time: 1 min; Temp: $600^{\circ}C$; Height: 1.5 mm; salt: 1 : 1 : 0.1 ($FeCl_2 : Ge : KI$)]	10 cm gives good crystals
6	H_2 gas ratio	5 sccm, 20 sccm, 40 sccm; [Dual time: 1 min; Temp: $600^{\circ}C$; Height: 1.5 mm; Te distance: 10 cm; salt: 1 : 1 : 0.1 ($FeCl_2 : Ge : KI$)]	No noticeable change among three H_2 gas ratio so 5 sccm is good enough
7	Substrate	SiO_2, mica [Dual time: 1 min; Temp: $600^{\circ}C$; Height: 1.5 mm; Te distance: 10 cm; salt: 1 : 1 : 0.1 ($FeCl_2 : Ge : KI$); H_2 gas ratio: 5 sccm]	More experiments need to be done to confirm the result

Figure 3.5: CVD Summary Table.

3.3 Raman Spectra of FGT

To start the primary characterizations, we started to do the image analysis using the optical microscope from Hui Cai's lab. The size of the crystals and crystal edges were measured using the optical microscope. To determine the vibrations of different phonon modes of FGT we started to take Raman spectra from crystals of different optical contrast on both SiO_2 and mica substrate using the Horiba Raman spectrometer of $532nm$ laser wavelength. The Raman spectra of bulk FGT on the mica substrate was very clear which confirms that the crystals that we produced are FGT. To identify the Raman modes of FGT we compared our spectra from literature. Our Raman spectra from FGT match from experimental works [23] and therefore, confirm that the crystals that we are producing are FGT.

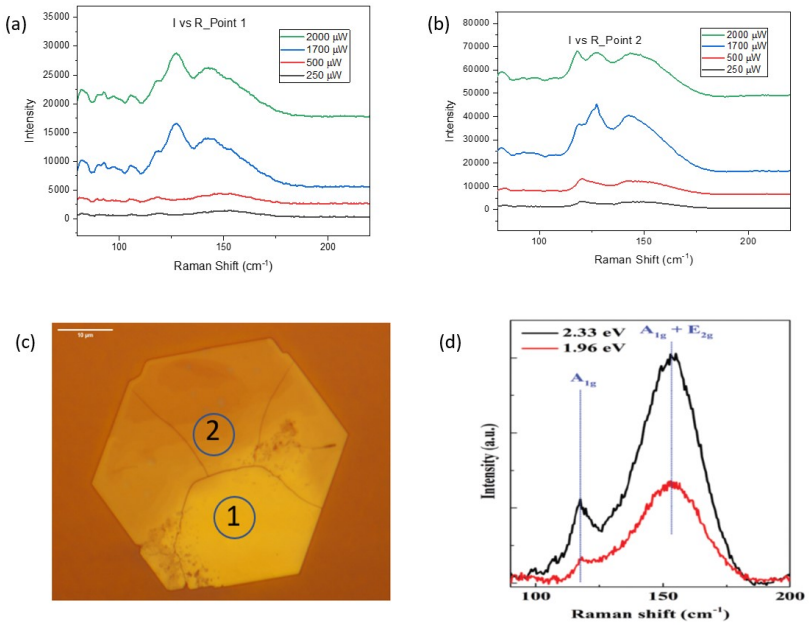

Figure 3.6: Raman Spectra from two different points F3GT crystal shown in figure (c) synthesized on SiO_2 substrate using the Raman spectrometer from Hui Cai lab (Figures (a) and (b)). The E_{1g}, A_{1g}, and E_{2g} modes appeared at lower laser powers (250 and 500) match with the spectra from literature (figure (d)) [23].

While Raman spectroscopy is an effective technique for examining a material's vibrational characteristics, it is not suitable for characterization of ferromagnetic materials, such as FGT. One of the key drawbacks is that Raman spectroscopy

cannot reveal information about the magnetic ordering of the material because it is insensitive to magnetic characteristics. Raman spectroscopy's sensitivity to surface changes limits its ability to examine the characteristics of the material's uppermost atomic layers. This can be problematic when studying thin films or multilayered materials since the properties of the surface layers may be different from those of the bulk material. Besides, The percentage concentration and chemical states of a material's constituent parts cannot be studied using Raman spectroscopy. X-ray Photoelectron Spectroscopy (XPS) is a surface-sensitive technique that can determine a material's constituent elements and chemical states, helps get around this. This approach is highly effective as it not only displays the elements present but also the elements to which they are bonded to. This information may be utilized to investigate chemical processes in a variety of materials, including metals, semiconductors, and insulators. XPS offers several benefits, including comprehensive elemental composition, empirical formula, chemical state, and electronic state profiling of the elements present on the surface of the material. Results of the XPS depth profiling of FGT are presented in the following section.

3.4 XPS Depth Profiling of FGT

The XPS of Iron Germanium Telluride (FGT) has been studied followed by different synthesis methods including exfoliation, sputtering, solid-state reaction, solid phase sintering and recrystallization (vapor transport), and chemical vapor deposition [5, 8, 9, 10, 12, 13, 14]. The different synthesis strategies of FGT have been discussed in chapter 2. In this section, the XPS results from different etching levels of the produced samples have been discussed. According to the most recent work of the synthesis of FGT via CSCVD reaction Fe_3GeTe_2 was obtained when the Fe:Ge ratio in the precursor was 1:1. When the Fe:Ge precursor ratio in the precursor was 2:1 and 3:1, Fe_5GeTe_2 was obtained. The XPS results of our samples are similar to some recent works [11, 10, 9, 12] including the work on CVD [5] but none of them showed the depth profiling results at different etching levels like we did here. The percentage concentration of different precursor substances with the

stoichiometric ratios from multiple etching levels after some time interval is also presented.

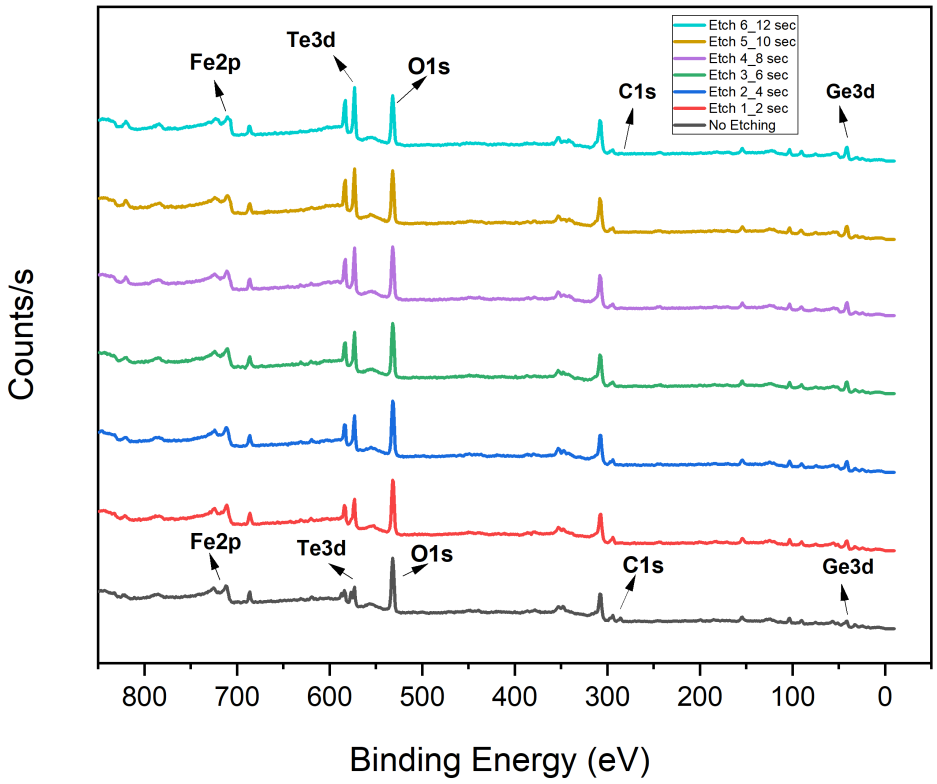

Figure 3.7: Survey spectra from XPS depth profile of Iron Germanium Telluride (Fe_5GeTe_2) from the CVD growth $2:1:0.1$ ($FeCl_2 : Ge : KI$) molar ratio on the mica substrate.

3.4.1 XPS Results from 2:1:0.1 ($FeCl_2 : Ge : KI$) molar ratio

The XPS analysis was performed using an AXIS Supra spectrometer (Kratos Analytical, UK) equipped with a hemispherical analyzer and a monochromatic Al K-alpha source ($1,444.6eV$). The peak positions and oxidation states of elements were identified by Rajendran et al.. [5]. The XPS survey spectra in figure 3.7 show clear iron, germanium, and tellurium peaks with some other elements like

oxygen, and carbon which are indicated with arrows. The binding energies (BEs) for all spectra were charge-corrected based on the C 1s for C-C bond at 284.8 eV. Oxygen from O1s orbital is present at all etching levels which is an evidence of the formation of a hybrid of Fe_5GeTe_2 and an oxide layer. The peak fittings were done using the XPSPeakFit software and all the plottings were done in Origin.

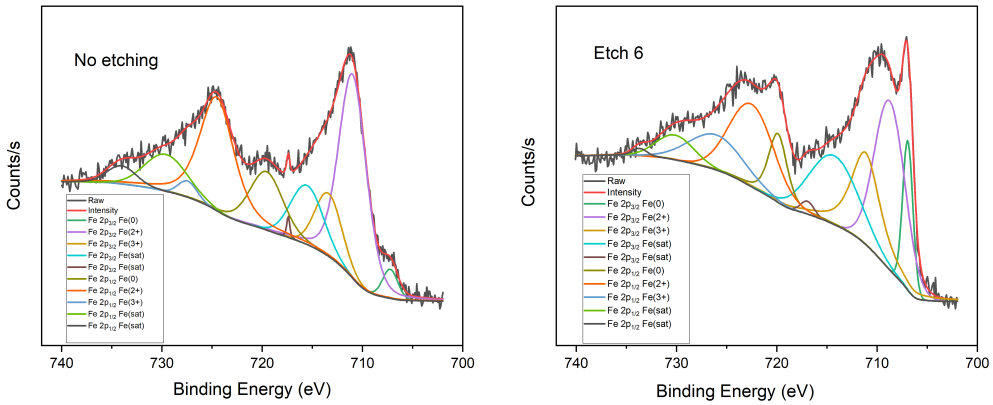

Figure 3.8: Fe2p Spectra show spin-orbit splitting ($Fe2p_{1/2}$, and $Fe2p_{3/2}$) before and after etching from the CVD growth of 2:1:0.1 ($FeCl_2 : Ge : KI$) molar ratio on the mica substrate.

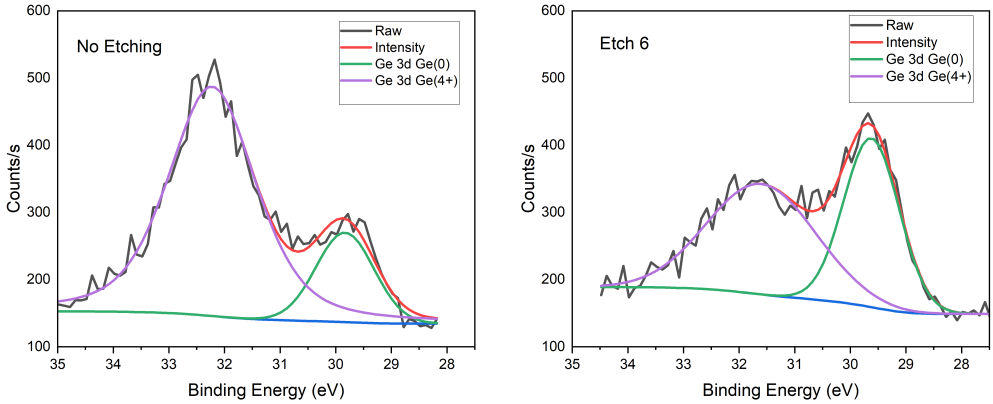

Figure 3.9: Ge3d Spectra do not show spin-orbit splitting before and after etching from the CVD growth of 2:1:0.1 ($FeCl_2 : Ge : KI$) molar ratio on the mica substrate.

Figure 3.8 represents the Fe elemental (Fe^0), $Fe2p_{1/2}$, and $Fe2p_{3/2}$ mixed valence oxidation states of Fe in FGT before and after etching. The Fe 2p zero

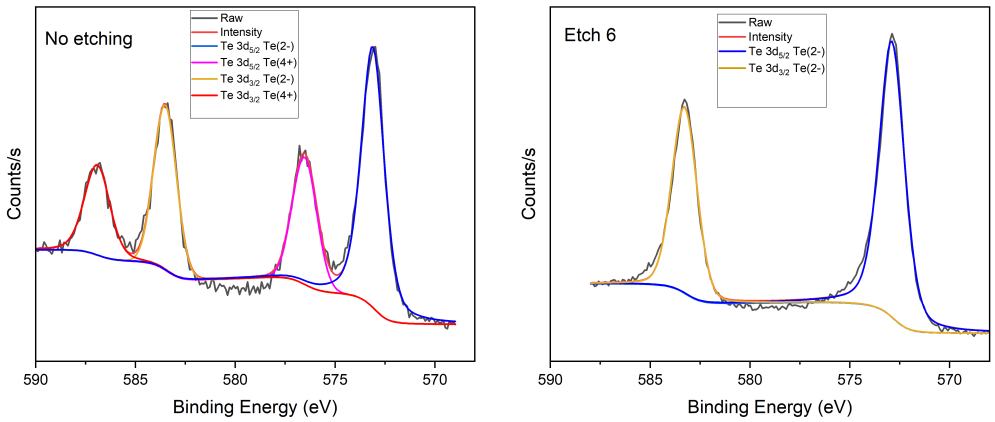

Figure 3.10: Te3d Spectra shows spin-orbit splitting ($Te3d_{3/2}$, and $Te3d_{5/2}$) before and after etching from the CVD growth of 2:1:0.1 ($FeCl_2 : Ge : KI$) molar ratio on the mica substrate.

valence band peak, Fe (2+) doublets ($Fe2p_{1/2}$,$Fe2p_{3/2}$), and Fe (3+) doublets ($Fe2p_{1/2}$,$Fe2p_{3/2}$) are observed along with their resonance transition (satellite peaks) at their corresponding binding energies. The presence of Fe^{2+} and Fe^{3+} doublet peaks suggests that Fe exists in ionic form with a mixed valence of +2 and +3 in the Fe_5GeTe_2 lattice. A very small amount of metallic phase ($Fe2p_{3/2}$ and $Fe2p_{1/2}$ before and after etching) could also be detected, although this could be impurity phase present within the analysis area but located outside the flakes. Similarly, The analysis of the Ge 3d5/2 and Ge 3d3/2 peaks in Figure 3.9 reveals that Ge is present as both elemental Ge (Ge^0), and Ge (4+) species in Fe_5GeTe_2, only the latter is used to determine the composition. Telluride Phase (i.e., Te(2-)) in the Te 3d spectra with spin-orbit splitting at Te 3d5/2 eV and Te 3d3/2 is presented in figure 3.10 and was considered in the elemental analysis. The peak positions with FWHM of all peaks that appear in Fe_5GeTe_2 are presented in the appending table A.2. It is noted that all peaks at Etching level 6 were shifted to a lower binding energy site which is also found in the literature [9].

The origin of the doublet peaks in spin-orbit splitting starts with the Hund's rule. From quantum mechanics, an electron in an atomic orbital can be labelled by four quantum numbers $|n, l, l_z, \sigma_z >$. For an isolated atom there is a set of rules, known as "Hund's Rules", which determines how the electrons fill orbitals and

what spin states they take, and hence whether the atom has a magentic moment.

Hund's First Rule (paraphrased): Electrons try to align their spins.

Hund's Second Rule (paraphrased): Electrons try to maximize their total orbital angular momentum, consistent with Hund's first rule.

Hund's Third Rule (paraphrased): Given Hund's first and second rules, the orbital and spin angular momentum either align or antialign, so that the total angular momentum is $J = |l \pm s|$ with the sign being determined by whether the shell of orbitals is more than half filled (+) or less than half filled (-).

Core levels in XPS use the nomenclature nl_j where n is the principal quantum number, l is the angular momentum quantum number and $j = l \pm s$ (where s is the spin angular momentum number and can be $\pm\frac{1}{2}$). All orbital levels except the s levels (l = 0) give rise to a doublet with the two possible states having different binding energies. This is known as spin-orbit splitting. The j values for different subshells are as follows.

Table 3.2: J values from different sub shells.

Subshells	l values	s values	J values
s	0	$\pm\frac{1}{2}$	$\frac{1}{2}$
p	1	-	$\frac{1}{2}, \frac{3}{2}$
d	2	-	$\frac{3}{2}, \frac{5}{2}$
f	3	-	$\frac{5}{2}, \frac{7}{2}$

The doublet peaks in spin-orbit splitting can be identified by separation constraints and area constraints. The Fe2p spectra can be deconvoluted into ten peaks before and after etching as shown in figure 3.8 similar to Rajendran et al [5]. There is an abundance of +2 oxidation state of Fe especially at the surface before etching and at etching level 1 which eventually decreases with time at a higher etching level ensuring the formation of more $Fe-Te$ bonds with an increase of Te deposition in the material (see table 3.3). We are observing strong Fe metallic peaks after etching similar to the literature [9, 10]. No spin-orbit splitting was found in Germanium peaks before and after etching as shown in figure 3.9. The Tellurium

on the surface formed TeO_2 with Te^{4+} which was not found at etching level 6 where the Tellurium percentage was maximum. The percentage concentration (Conc..) of Germanium decreases with an increase in the concentration of tellurium (Te) revealing a possibility of Te terminated atomic structure of FGT which should be confirmed with further characterization in future.

Table 3.3: Results from XPS Depth Profiling of 2:1:0.1 ($FeCl_2 : Ge : KI$) ratio on mica substrate.

No	Level of Etching	% Conc.. Fe^{2+}	% Conc.. Fe^{3+}	% Conc.. Ge^{4+}	% Conc.. Te^{2-}	$\frac{Fe^{2+}}{Fe^{3+}}$ Ratio	Stoichiometric Ratio
1	Etch0 0 sec	51.6	9.5	28.48	10.43	5.43	$Fe_{2.15}GeTe_{0.37}$
2	Etch1 2 sec	55.96	4.94	23.97	15.14	11.32	$Fe_{2.54}GeTe_{0.63}$
3	Etch2 4 sec	41.4	22.31	17.72	18.56	1.86	$Fe_{3.59}GeTe_{1.05}$
4	Etch3 6 sec	39.87	20.07	18.74	21.32	1.99	$Fe_{3.20}GeTe_{1.14}$
5	Etch4 8 sec	34.39	25.81	15.98	23.81	1.33	$Fe_{3.77}GeTe_{1.49}$
6	Etch5 10 sec	45.34	16.82	15.43	22.41	2.7	$Fe_{4.02}GeTe_{1.45}$
7	Etch6 12 sec	37.42	22.72	12.72	27.15	1.65	$Fe_{4.73}GeTe_{2.13}$

The basic tool for measuring the number of electrons recorded for an atomic state is the quantification region. The underlying assumption when quantifying XPS spectra is that the number of electrons recorded is proportional to the number of atoms in a given state. Table 3.3 shows changes in the atomic precentages of Fe, Ge, and Te suggesting alterations in their coordination state and potential impacts on their magnetic properties. The XPS calculation of percentage concentration with the stoichiometric ratio (SR) is shown in the appendix. In the appendix, table A.2 represents the peak positions with Full Width at Half Maximum (FWHM). It is found that almost all peaks shifted to a lower energy site after etching (etch 6) which is sililar to the literature [9].

Finally, the XPS results showed that the chemical states of each element in

CSCVD method [5] were maintained in our version, suggesting that properties like magnetism, which depend on the nearest neighboring interaction, could also be preserved. However, the concentration of Fe^{2+} is higher compared to Rajendran's work which could affect the material's properties. It is to be noted that the thickness of XPS surface by Rajendran et al is unknown and the percentage concentration of iron as well as the material's properties could vary with thickness. Therefore, Atomic Force Microscopy to measure the thickness of the Fe_5GeTe_2 flakes before and after the etching of XPS depth profiling is important and should be done in the future.

Chapter 4

Synthesis of Ni Doped Iron Germanium Telluride

4.1 Chemical Vapor Deposition of Ni doped FGT

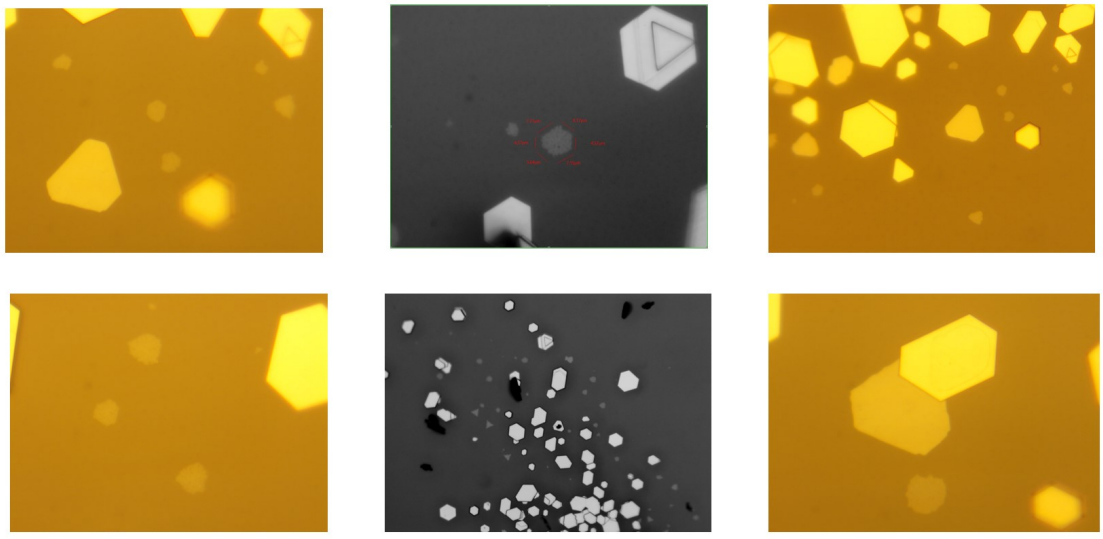

Figure 4.1: Images of Ni doped Iron Germanium Telluride on mica substrate.

4.1.1 Method

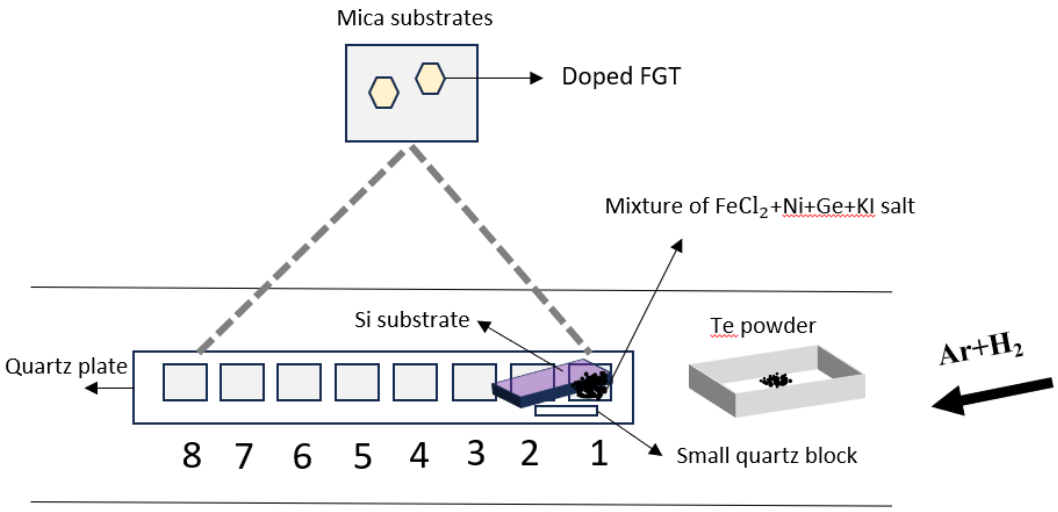

Figure 4.2: CVD Schematic FNiGT

I started to synthesize FGT doped with Ni powders on both SiO_2 and mica substrate. The growth method on the SiO_2 substrate was exactly same as the method to grow F3GT in chapter 3. The method was a little bit different on the mica substrate. For this, we placed a high amount of precursors on top of one mica substrate at the zone center. Seven other mica substrates were placed besides the precursors substrate at the downstream side keeping a 1 cm distance between them where the first two were covered with a top SiO_2 substrate creating a cascaded environment by tilting the top SiO_2 substrate at a small angle using a quartz block of 1.5 mm height. All mica substrates were placed on a quartz plate. The precursors ratio is 2:1:0.1 for $FeCl_2$, Ge, and KI salt respectively. Ni powders were added in a percentage of 5%, 10%, 20% to understand the effect of doping in a varying amount.

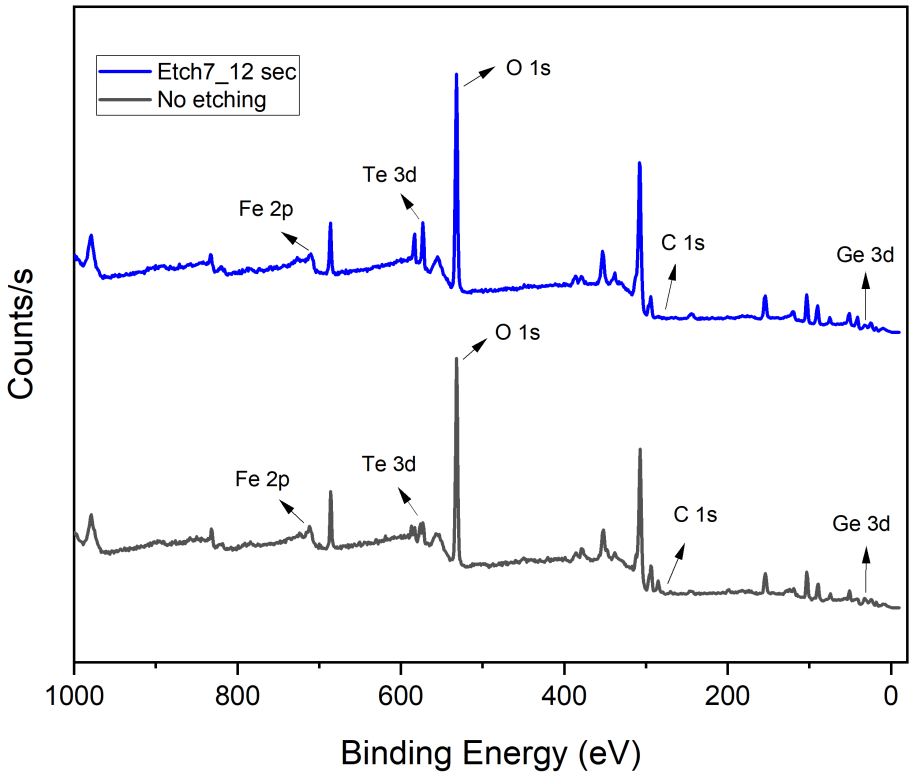

Figure 4.3: Survey spectra from XPS depth profile of Ni-doped Iron Germanium Telluride ($Fe_{3.6}Ni_{0.47}TeGe_{1.95}$) from the CVD growth 2:1:0.1 ($FeCl_2 : Ge : KI$) molar ratio on the mica substrate.

4.2 X-ray Photoelectron Spectroscopy of Ni doped FGT

To examine the XPS results of Ni doped bulk films of the samples were selected from the second mica substrate from the precursors substrate on the downstream side. The selected precursors ratio was $2 : 1 : 0.2 : 0.1$ ($FeCl_2 : Ge : Ni : KI$). The XPS spectra from Nickel (Ni) element was identified and confirmed from the literature [24, 8, 25]. Ni is substituting to the (Fe^{2+}) in the material which is discussed in the next section. There is no literature evidence on the XPS of FGT with Ni doping because no work has been done on the synthesis of FGT with Ni doping directly on a substrate through Chemical Vapor Deposition (CVD). The

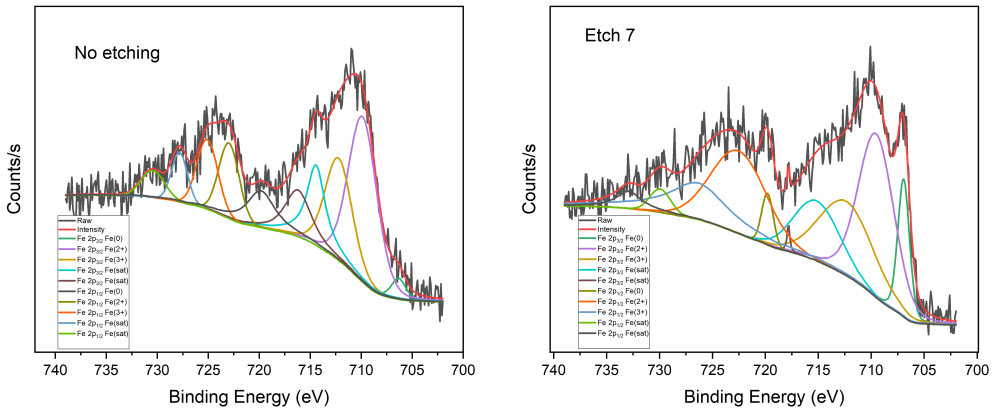

Figure 4.4: Fe2p Spectra show spin-orbit splitting ($Fe2p_{1/2}$, and $Fe2p_{3/2}$) before and after etching from the CVD growth of 2:1:0.2:0.1 ($FeCl_2 : Ge : Ni : KI$) molar ratio on the mica substrate.

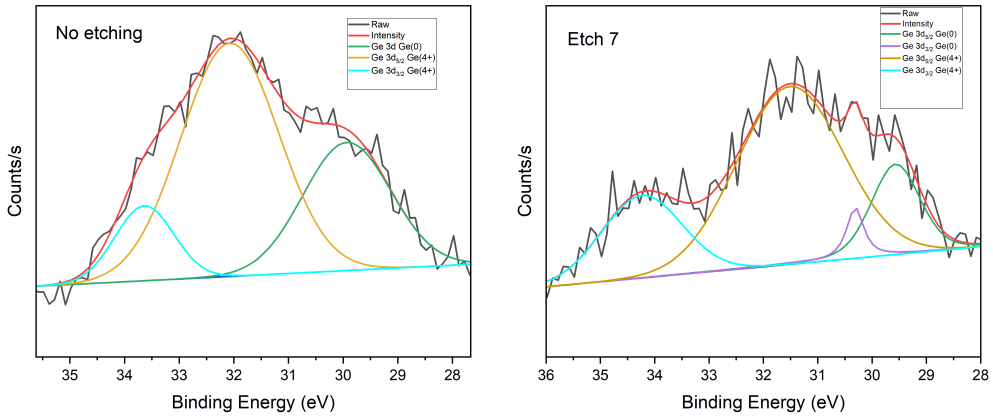

Figure 4.5: Ge3d Spectra show spin-orbit splitting ($Ge3d_{3/2}$, and $Ge3d_{5/2}$) before and after etching from the CVD growth of 2:1:0.2:0.1 ($FeCl_2 : Ge : Ni : KI$) molar ratio on the mica substrate.

details of XPS results including the survey plot and other spectra of the elements are discussed below.

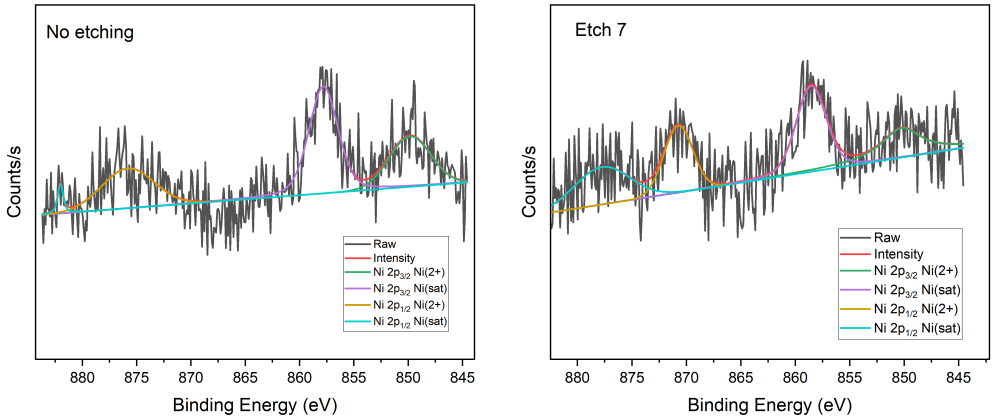

Figure 4.6: Ni2p Spectra show spin-orbit splitting ($Ni2p_{1/2}$, and $Ni2p_{3/2}$) before and after etching from the CVD growth of 2:1:0.2:0.1 ($FeCl_2 : Ge : Ni : KI$) molar ratio on the mica substrate.

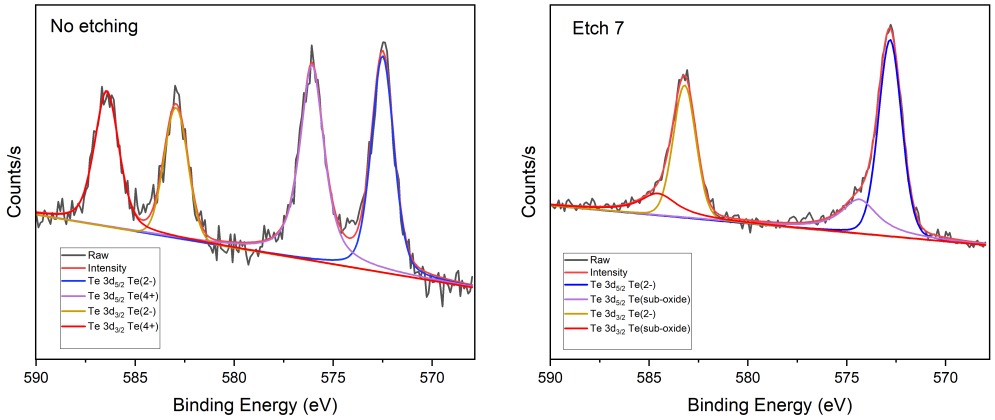

Figure 4.7: Te3d Spectra shows spin-orbit splitting ($Te3d_{3/2}$, and $Te3d_{5/2}$) before and after etching from the CVD growth of 2:1:0.2:0.1 ($FeCl_2 : Ge : Ni : KI$) molar ratio on the mica substrate.

4.2.1 XPS Results from 2:1:0.2:0.1 ($FeCl_2 : Ge : Ni : KI$) molar ratio

The survey spectra in figure 4.4 represent all the peaks including iron (Fe), germanium (Ge), nickel (Ni), and tellurium (Te). The oxygen from O1s is strong, similar to figure 3.7, confirming the formation of a hybrid form of Ni-doped FGT and oxide layer. Figure 4.4 represents the Fe spectra from Ni doped FGT. The

Table 4.1: Results from XPS Depth Profiling of 2:1:0.2:0.1 ($FeCl_2 : Ge : Ni : KI$) ratio at 10 cm Te distance on mica substrate.

No	Level of Etching	% Conc.. Fe^{2+}	% Conc.. Fe^{3+}	% Conc.. Ni^{2+}	% Conc.. Ge^{4+}	% Conc.. Te^{2-}	$\frac{Fe^{2+}}{Fe^{3}+}$ Ratio	Stoichiometric Ratio
1	Etch0 0 sec	24.67	16.44	9.73	41.77	7.4	1.5	$Fe_{5.55}Ni_{1.31}TeGe_{5.64}$
2	Etch 5 10 sec	31.1	10.13	6.02	39.52	13.24	3.07	$Fe_{3.11}Ni_{0.45}TeGe_{2.99}$
3	Etch 6 12 sec	34.16	11.44	5.97	33.9	14.54	2.99	$Fe_{3.18}Ni_{0.41}TeGe_{2.33}$
4	Etch 7 14 sec	30.5	20.73	6.74	27.78	14.24	1.47	$Fe_{3.6}Ni_{0.47}TeGe_{1.95}$
5	Etch 8 16 sec	26.1	14.72	10.79	32.87	15.54	1.77	$Fe_{2.52}Ni_{0.69}TeGe_{2.12}$

result is quiet similar to the Fe spectra from Fe_5GeTe_2 except a major decrease in the $\frac{Fe^{2+}}{Fe^{3+}}$ value (from 5.43 down to 1.5) on the surface (no etching) indicating that Ni is substituting to the Fe^{2+} atom forming $Ni - Te$ bond. The peak positions of all the peaks (see appendix table B.1) are comparable to the previous results in chapter 3 (see appendix table A.2) where no doping was present.

Figure 4.5 show spin-orbit splitting of Ge^{4+} peaks before and after etching as mentioned in the caption. Besides, the peak position of the $Ge3d_{5/2}$ shifted to higher binding energy. The reason for this shift is unknown and could be related to the addition of Ni doping in the system. The Ni2p spectra were compared with the XPS results of $NiTe$, $NiGeTe_3$, and other Ni doped material in the literature [24, 8, 25]. We are observing clear ($Ni2p_{1/2}$, and $Ni2p_{3/2}$) peaks with their resonance peaks in figure 4.6. From figure 4.7 we can see that peaks from TeO_2 is very strong at the surface (before etching). The ion sputtering process also caused partial decomposition of tellurium oxide to suboxide (etch 7) indicating changes in the chemical state of the material at that level. The peak positions with

FWHM are shown in the appendix table B.1.

Finally, from table 4.1 we can see a stable formation of Ni-doped FGT with a stoichiometric ratio of $Fe_{3.6}Ni_{0.47}TeGe_{1.95}$ at etching level 7. The result is different from Fe_5GeTe_2 because Germanium is the most abundant on the surface (no etching). This strong surface germanium indicates a Ge-terminated atomic structure of the doped sample. Although the percentage concentration of Ge decreases with the level of etching but it is still much higher than the percentage concentration of Te which can change the atomic structure and properties of the material. Further structural, electronic, magnetic, and other characterizations are required to confirm this.

4.3 Future Works

From the above discussion, It is obvious that the magnetic properties of FGT could be dramatically change in presence of doping in a different manner. Therefore, tuning the magnetic characteristics of Iron Germanium Telluride (FGT) will produce novel, intriguing outcomes in the future and will lead to the better understanding of many fundamental questions with possible new path to real world device applications.

More synthesis should be done with higher Ni doping values on FGT. Besides, the thickness of both undoped and doped films should be measured by Atomic Force Microscope. Magnetic force Microscope measurements could reveal new magnetic domains in the sample. The structural characterization should be done by HAADF STEM measurements. The Physical property like the Curie temperature of the material should be measured in a Physical Property Measurement system. Overall, the synthesis of FGT and Ni-doped FGT could reveal new significant properties of the materials which could be used for spintronic applications.

Appendix A

XPS Calculation and Peak Positions Table of FGT

A general Expression for determining the atom fraction of any constituent in a sample, C_x, can be written as,

$$C_x = \frac{n_x}{n_i} = \frac{I_x/S_x}{\Sigma I_i/S_i} \tag{A.1}$$

where I_x is the no of photoelectrons in the sample and S_x is the relative sensitivity factor of the sample.

The calculation of the percentage concentration of Fe_5GeTe_2 is listed below.

Table A.1: XPS Calculation for Fe_5GeTe_2

No	Material	I_x	S_x	I_x/S_x	$\Sigma I_i/S_i$	C_x	SR
1	$Fe2p$	20969.25	14.35	1461.07	2429.49	0.60	$Fe_{4.73}GeTe_{2.13}$
2	$Ge3d$	399.74	1.29	308.92	2429.49	0.13	-
3	$Te3d$	27918.62	42.33	659.5	2429.49	0.27	-

Table A.2: Peak positions, full width at half maximum (FWHM), and χ^2 values for Fe2p, Ge3d, and Te3d from XPS Depth Profiling of 2:1:0.1 ($FeCl_2 : Ge : KI$) molar ratio in the powdered mixture at 10 cm Te distance directly on the mica substrate.

Sample Fe_5GeTe_2

Treatment	Species	Peak Positions	FWHM	χ^2 values
Etch 0	Fe^0	707.232, 719.572	1.776, 3.881	0.74
	Fe^{2+}	710.99, 724.52	3.232, 4.033	-
	Fe^{3+}	713.395, 727.432	3.139, 2.17	-
	Fe^{2+} Satellites	715.533, 729.592	3.815, 4.999	-
	Fe^{3+} Satellites	717.401, 734.022	0.368, 3.422	-
	Ge^0	29.834	1.228	1.17
	Ge^{4+}	32.223	1.852	-
	Te^{2-}	573.108, 583.510	1.356, 1.344	2.54
	Te^{4+}	576.526, 586.914	1.437, 1.509	-
Etch 6	Fe0	706.945, 719.893	1.198, 2.194	0.82
	Fe2+	708.744, 722.517	3.593, 5.233	-
	Fe3+	711.144, 726.042	3.382, 6.386	-
	Fe^{2+} Satellites	714.278, 730.156	5.737, 4.377	-
	Fe^{3+} Satellites	716.958, 733.686	1.567, 1.742	-
	Ge0	29.62	1.174	0.77
	Ge4+	31.6	2.285	-
	Te2-	572.89, 583.281	1.506, 1.471	7.5

Appendix B

Peak Positions Table of Ni Doped FGT

The XPS Calculation procedure of Ni doped FGT is same except there is an extra element (Ni) in the doped sample. The Relative Sensitivity Factor (RSF) for Ni 2P is 20.764.

Table B.1: Peak positions, full width at half maximum (FWHM), and χ^2 values for Fe2p, Ge3d, and Te3d from XPS Depth Profiling of 2:1:0.2:0.1 ($FeCl_2 : Ge : Ni : KI$) molar ratio in the powdered mixture at 10 cm Te distance directly on the mica substrate.

Sample $Fe_{3.6}Ni_{0.47}TeGe_{1.95}$

Treatment	Species	Peak Positions	FWHM	χ^2 values
Etch 0	Fe^0	706.327, 719.816	1.671, 2.357	0.74
	Fe^{2+}	709.866, 722.970	3.317, 2.433	-
	Fe^{3+}	712.209, 725.090	3.125, 1.828	-
	Fe^{2+} Satellites	714.424, 727.817	2.172, 1.828	-
	Fe^{3+} Satellites	716.190, 730.421	3.023, 2.635	-
	Ni^{2+}	849.834, 875.801	4.503, 5.664	0.75
	Ni Satellites	857.801, 882.012	3.169, 0.584	-
	Ge^0	29.932	1.89	0.59
	Ge^{4+}	32.075, 33.64	2.102, 1.264	-
	Te^{2-}	572.5, 582.937	1.337, 1.414	0.97
	Te^{4+}	576.067, 586.432	1.445, 1.463	-
Etch 6	Fe0	706.932, 719.797	1.301, 1.275	0.77
	Fe2+	709.531, 722.522	3.983, 6.118	-
	Fe3+	712.339, 726.311	6.013, 6.647	-
	Fe^{2+} Satellites	715.144, 729.930	5.124, 2.295	-
	Fe^{3+} Satellites	717.819, 732.895	0.282, 2.844	-
	Ni^{2+}	850.236, 870.737	4.455, 3.118	0.83
	Ni Satellites	858.535, 877.741	3.231, 5.957	-
	Ge0	29.567, 30.310	1.051, 0.380	0.78
	Ge4+	31.511, 34.238	2.287, 1.740	-
	Te2-	572.805, 583.206	1.380, 1.354	0.81
	Te sub-oxide	574.361, 584.542	2.245, 2.287	-

Bibliography

[1] David L Cortie, Grace L Causer, Kirrily C Rule, Helmut Fritzsche, Wolfgang Kreuzpaintner, and Frank Klose. Two-dimensional magnets: forgotten history and recent progress towards spintronic applications. *Advanced Functional Materials*, 30(18):1901414, 2020.

[2] Xue Jiang, Qinxi Liu, Jianpei Xing, Nanshu Liu, Yu Guo, Zhifeng Liu, and Jijun Zhao. Recent progress on 2d magnets: Fundamental mechanism, structural design and modification. *Applied Physics Reviews*, 8(3):031305, 2021.

[3] Bijun Tang, Dianyi Hu, Xiaoxu Zhao, Xiaowei Wang, and Zheng Liu. Recent developments in chemical vapor deposition of 2d magnetic transition metal chalcogenides. *ACS Applied Electronic Materials*, 4(7):3303–3324, 2022.

[4] Marco Gibertini, Maciej Koperski, Alberto F Morpurgo, and Konstantin S Novoselov. Magnetic 2d materials and heterostructures. *Nature nanotechnology*, 14(5):408–419, 2019.

[5] Govindan Kutty Rajendran Nair, Zhaowei Zhang, Fuchen Hou, Ali Abdelaziem, Xiaodong Xu, Steve Wu Qing Yang, Nan Zhang, Weiqi Li, Chao Zhu, Yao Wu, et al. Phase-pure two-dimensional fe x gete2 magnets with near-room-temperature tc. *Nano Research*, 15(1):457–464, 2022.

[6] Zaiyao Fei, Bevin Huang, Paul Malinowski, Wenbo Wang, Tiancheng Song, Joshua Sanchez, Wang Yao, Di Xiao, Xiaoyang Zhu, Andrew May, et al. Two-dimensional itinerant ising ferromagnetism in atomically thin fe3gete2, 1803.

[7] Hui Li, Shuangchen Ruan, and Yu-Jia Zeng. Intrinsic van der waals magnetic materials from bulk to the 2d limit: new frontiers of spintronics. *Advanced Materials*, 31(27):1900065, 2019.

[8] Filipa M Oliveira, Nikolas Antonatos, Vlastimil Mazánek, David Sedmidubskỳ, Zdeněk Sofer, and Rui Gusmão. Exfoliated fe3gete2 and ni3gete2 materials as water splitting electrocatalysts. *FlatChem*, 32:100334, 2022.

[9] Suping Ma, Guanghao Li, Zhuo Li, Yawen Zhang, Haolin Lu, Zhansheng Gao, Jinxiong Wu, Guankui Long, and Yi Huang. 2d magnetic semiconductor fe3gete2 with few and single layers with a greatly enhanced intrinsic exchange bias by liquid-phase exfoliation. *ACS nano*, 16(11):19439–19450, 2022.

[10] Guanghao Li, Suping Ma, Zhuo Li, Yawen Zhang, Jianglin Diao, Lun Xia, Zhiwei Zhang, and Yi Huang. High-quality ferromagnet fe3gete2 for high-efficiency electromagnetic wave absorption and shielding with wideband radar cross section reduction. *ACS nano*, 16(5):7861–7879, 2022.

[11] Qianwen Zhao, ChaoChao Xia, Hanying Zhang, Baiqing Jiang, Tunan Xie, Kaihua Lou, and Chong Bi. Ferromagnetism of nanometer thick sputtered fe3gete2 films in the absence of two-dimensional crystalline order: Implications for spintronics applications. *ACS Applied Nano Materials*, 6(4):2873–2882, 2023.

[12] Andrew F May, Dmitry Ovchinnikov, Qiang Zheng, Raphael Hermann, Stuart Calder, Bevin Huang, Zaiyao Fei, Yaohua Liu, Xiaodong Xu, and Michael A McGuire. Ferromagnetism near room temperature in the cleavable van der waals crystal fe5gete2. *ACS nano*, 13(4):4436–4442, 2019.

[13] Amir A Rezaie, Eunsoo Lee, Diana Luong, Johan A Yapo, and Boniface PT Fokwa. Abundant active sites on the basal plane and edges of layered van der waals fe3gete2 for highly efficient hydrogen evolution. *ACS Materials Letters*, 3(4):313–319, 2021.

[14] Eunsoo Lee, Amir A Rezaie, Diana Luong, Johan A Yapo, and Boniface PT Fokwa. Fe5ge2te2: Iron-rich layered chalcogenide for highly efficient hydrogen evolution. *Zeitschrift für anorganische und allgemeine Chemie*, 648(15):e202200066, 2022.

[15] Luzhao Sun, Guowen Yuan, Libo Gao, Jieun Yang, Manish Chhowalla, Meysam Heydari Gharahcheshmeh, Karen K Gleason, Yong Seok Choi, Byung Hee Hong, and Zhongfan Liu. Chemical vapour deposition. *Nature Reviews Methods Primers*, 1(1):5, 2021.

[16] Bevin Huang, Michael A McGuire, Andrew F May, Di Xiao, Pablo Jarillo-Herrero, and Xiaodong Xu. Emergent phenomena and proximity effects in two-dimensional magnets and heterostructures. *Nature Materials*, 19(12):1276–1289, 2020.

[17] Hang Xu, Shengjie Xu, Xun Xu, Jincheng Zhuang, Weichang Hao, and Yi Du. Recent advances in two-dimensional van der waals magnets. *Microstructures*, 2:2022011, 2022.

[18] YJ Deng, YJ Yu, YB Zhang, Yujun Deng, Yijun Yu, Yichen Song, Jingzhao Zhang, Nai Zhou Wang, Zeyuan Sun, Yangfan Yi, Yi Zheng Wu, Shiwei Wu, Junyi Zhu, Jing Wang, Xian Hui Chen, and Yuanbo Zhang. Gate-tunable room-temperature ferromagnetism in two-dimensional fe3gete2. *Nature.*, 563(7729):94, 2018-11.

[19] Rajeswari Roy Chowdhury, Samik DuttaGupta, Chandan Patra, Oleg A Tretiakov, Sudarshan Sharma, Shunsuke Fukami, Hideo Ohno, and Ravi Prakash Singh. Unconventional hall effect and its variation with co-doping in van der waals fe3gete2. *Scientific reports*, 11(1):1–10, 2021.

[20] Xiang Chen, Yu-Tsun Shao, Rui Chen, Sandhya Susarla, Tom Hogan, Yu He, Hongrui Zhang, Siqi Wang, Jie Yao, Peter Ercius, et al. Pervasive beyond room-temperature ferromagnetism in a doped van der waals magnet. *Physical review letters*, 128(21):217203, 2022.

[21] Gil Drachuck, Zaher Salman, Morgan W Masters, Valentin Taufour, Tej N Lamichhane, Qisheng Lin, Warren E Straszheim, Sergey L Bud'Ko, and Paul C Canfield. Effect of nickel substitution on magnetism in the layered van der waals ferromagnet fe 3 gete 2. *Physical Review B*, 98(14):144434, 2018.

[22] Cong-Kuan Tian, Cong Wang, Wei Ji, Jin-Chen Wang, Tian-Long Xia, Le Wang, Juan-Juan Liu, Hong-Xia Zhang, and Peng Cheng. Domain wall pinning and hard magnetic phase in co-doped bulk single crystalline fe 3 gete 2. *Physical Review B*, 99(18):184428, 2019.

[23] Fangfang Cui, Xiaoxu Zhao, Junjie Xu, Bin Tang, Qiuyu Shang, Jianping Shi, Yahuan Huan, Jianhui Liao, Qing Chen, Yanglong Hou, et al. Controlled growth and thickness-dependent conduction-type transition of 2d ferrimagnetic cr2s3 semiconductors. *Advanced Materials*, 32(4):1905896, 2020.

[24] Karthik S Bhat, Harish C Barshilia, and HS Nagaraja. Porous nickel telluride nanostructures as bifunctional electrocatalyst towards hydrogen and oxygen evolution reaction. *international journal of hydrogen energy*, 42(39):24645–24655, 2017.

[25] Jin Wang, Yimin Xuan, and Kai Zhang. Nickel doping as an effective strategy to promote separation of photogenerated charge carriers for efficient solar-fuel production. *Catalysis Science & Technology*, 11(12):4012–4015, 2021.